공학박사학위논문

자유낙하하는 단풍씨앗의 수치해석 연구

Numerical study of a freely-falling maple seed

2016 년 8 월

서울대학교 대학원

기계항공공학부

이 인 재

Numerical study of a freely-falling maple seed

Injae Lee
Department of Mechanical & Aerospace Engineering
Seoul National University

Abstract

Many winged seeds such as those of maples exploit autorotation to decrease the descending velocity and increase the dispersal distance for their conservation of species. In this study, we conduct numerical simulations of a freely-falling maple seed using an immersed boundary method in a non-inertial reference frame. A three-dimensional seed model is obtained by scanning a maple seed (*Acer palmatum*). The seed reaches a steady autorotation after a transient period. This transient period depends on the initial position of a seed and is shorter when the wing leading edge or nut or trailing edge of the seed is initially positioned upward. During autorotation, a stable leading-edge vortex is attached on the surface of the rotating seed. Two different approaches are considered to obtain scaling laws describing the relation among the seed weight and geometry, and descending and rotating velocities. The first uses the conservation of mass, linear and angular momentum, and energy. In this approach, a model constant to be determined, called the axial induction factor, is obtained from the result of present simulation. The second approach employs a classical steady wing theory in which the vortical strength is scaled with the circulation around a wing and the drag force is modeled by the time derivative of vortical impulse. Available data from winged seeds are applied to the present scaling

laws, showing excellent collapses onto the scaling laws.

Keywords: autorotation, maple seed, leading-edge vortex, scaling law, momentum theory, wing theory

Student number: 2008-20774

Contents

List of Figures

List of Tables

Nomenclature

Roman Symbols

a	axial induction factor
A_d	disk area, $A_d = \pi R_d^2$
A_w	wing planform area of the seed
AR	aspect ratio of the wing
c	mean chord length
C_D	drag coefficient
$C_{D,S}$	sectional drag coefficient
$\boldsymbol{f}$	momentum forcing
$\boldsymbol{F}_e$	external force on the body
$\boldsymbol{F}_I$	hydrodynamic force on the body in the inertial reference frame
$\boldsymbol{F}_N$	hydrodynamic force on the body in the non-inertial reference frame
Fr	froude number, $Fr = u_g/\sqrt{cg}$
g	gravitational acceleration
$\mathbf{I}_m$	principal moment of inertia of the body
k	RK3 substep index
D	drag force
m	mass of the seed
M_V	vortex impulse
p	pressure
q	mass source/sink
Q_m	transformation matrix for angular velocity

Re	Reynolds number, $Re = u_g c/\nu$
R_w	wing span of the seed
r_d	radial direction
R_d	radius of the disk
R_m	rotation matrix
$\boldsymbol{s}_a$ $(s_x,\, s_y,\, s_z)$	translational displacement of body
T	rotating period
t	time
$\boldsymbol{T}_e$	external moment on the body
$\boldsymbol{T}_I$	hydrodynamic moment on the body in the inertial reference frame
$\boldsymbol{T}_N$	hydrodynamic moment on the body in the non-inertial reference frame
$\boldsymbol{U}$	target velocity
U	incoming velocity
$\hat{\boldsymbol{u}}$	intermediate velocity
$\tilde{\boldsymbol{u}}$	provisional velocity
$\boldsymbol{u}_a$	velocity vector in the inertial reference frame
u_d	descending velocity of the seed
u_g	characteristic velocity, $u_g = \sqrt{(\rho - 1)cg}$
$\boldsymbol{u}_r$	velocity vector in the non-inertial reference frame
$\boldsymbol{u}_s$ $(u_s,\, v_s,\, w_s)$	linear velocity of the body in the non-inertial reference frame
u_T	terminal descending velocity of the seed
U_T	non-dimensional terminal descending velocity of the seed
u_z, u_r, u_θ	axial, radial, and circumferential velocities, respectively
$\boldsymbol{u}_\infty$	wind-velocity
$\boldsymbol{x}_a$	orthogonal coordinates in the inertial reference frame

$\boldsymbol{x}_r$	orthogonal coordinates in the non-inertial reference frame

Greek Symbols

α	angle of attack
β	coning angle
Γ	circulation
Δt	computational time step
θ	pitching angle
Θ $(\phi_n, \theta_n, \psi_n)$	Euler angles
λ	tip speed ratio, $\lambda = Rd\omega_T/u_T$
λ_r	local tip speed ratio, $\lambda_r = r_d\omega_T/u_T$
ν	kinematic viscosity
ρ	density ratio of seed to fluid densities, $\rho = \rho_s/\rho_f$
ϕ	pseudo pressure
$\boldsymbol{\Omega}$ $(\Omega_x, \Omega_y, \Omega_z)$	angular velocity of the body
ω_d	rotating velocity of the seed
ω_T	terminal rotating velocity of the seed
Ω_T	non-dimensional terminal rotating velocity of the seed
$\alpha_k, \gamma_k, \rho_k$	coefficients of RK3 substeps

Chapter 1

Introduction

Many plants spread their winged seeds by wind for their conservation of species (Augspurger, 1986; Nathan *et al.*, 2002). Each flying seed is designed to have a small descending velocity and to fly in the air as long as possible, according to their environmental conditions (Minami & Azuma, 2003). If the center of mass of a winged seed is located near the aerodynamic center of the wing, then the seeds glide during their descent, without any rotation (Azuma & Okuno, 1989). On the other hand, if the center of mass is located near an end of the wing, then the seeds descend with a rotational motion (i.e. autorotation) (Azuma & Yasuda, 1989). The autorotation is the continuous rotation of a body by the fluid-structure interaction without any external power, and examples of this phenomena are the windmills, anemometers, and certain tree fruits and seeds (Smith, 1971; Lugt, 1983). Many winged seeds such as those of maples exploit autorotation to decrease the descending velocity and increase the dispersal distance by wind (figure 1.1) (Augspurger, 1986; Seter & Rosen, 1992; Nathan *et al.*, 2002). When these seeds initially fall from their parent trees, the offset between the gravity acting at the center of mass and the resulting aerodynamic force creates a moment (Norberg, 1973). The spin is centered about a point near the center of mass, while the wing tip shows a helical path (figure 1.2). At equilibrium, the vertical force (drag) balances the weight of the seed, and the resultant components of the centrifugal force generate a moment which

is balanced by the moment created by the aerodynamic force (Norberg, 1973). Autorotating seeds have a simple configuration without neuromuscular control for driving as in animal flight (Norberg, 1973), and even those with damaged wing can still autorotate (Jakubik *et al.*, 2004; Varshney, Chang & Wang, 2012). It means that autorotating seeds have a mechanically robust design unlike the flapping or rotating-blade mechanism (Fregene & Bolden, 2010), and thus they fascinate many researchers to develop micro air vehicles (MAVs) equipped with sensors for the reconnaissance (Jameson *et al.*, 2012; Pounds & Singh, 2013), munition (Crimi, 1988), and atmospheric researches (Burke, 1988; Diaz-Silva, Sarigul-Klijn & Sarigul-Klijn, 2013; Pandolfi & Izzo, 2013).

The understanding of falling dynamics and aerodynamic characteristics of autorotating seeds is essential to reveal the evolutionary direction of autorotating seeds and develop autorotation-based MAVs. To explore characteristics of autorotating seeds, many experimental and theoretical studies have been conducted (Norberg, 1973; McCutchen, 1977; Green, 1980; Augspurger, 1986; Azuma & Yasuda, 1989; Rosen & Seter, 1991, 1992; Seter & Rosen, 1992; Yasuda & Azuma, 1997; Nathan *et al.*, 2002; Minami & Azuma, 2003; Jakubik *et al.*, 2004; Lenink *et al.*, 2009; Varshney, Chang & Wang, 2012; Salcedo *et al.*, 2013; Lee, Lee & Sohn, 2014; Rao, Hoysall & Gopalan, 2014; Seter & Rosen, 2014; Sunada *et al.*, 2015). Norberg (1973) conducted a comprehensive and detailed investigation of autorotating seeds theoretically including discussions of the transient stage of entering autorotation and the stability of autorotation. However, most of them considered only seeds at the periodic state or in the quiescent condition.

1.1 Previous studies on the autorotating seed: experiments

Autorotating seeds have low descending velocities (indicating high drag force) because of their fast rotating motions in spite of their small wing areas but large seed weights (Norberg, 1973; McCutchen, 1977; Azuma & Yasuda, 1989). They are considered to have efficient flight mechanism than other flying types of seeds (figure 1.3) (Augspurger, 1986; Lenink *et al.*, 2009). To elucidate the mechanism of their high drag, flows around rotating seeds were measured using digital particle image velocimetries (DPIVs), where the rotating motion was *a priori* given or guided by a string to prevent arbitrary motions of seeds (Lenink *et al.*, 2009; Salcedo *et al.*, 2013; Lee, Lee & Sohn, 2014). They demonstrated that autorotating seeds attain high drag by keeping a stable leading-edge vortex on the wing surface at periodic autorotation. It has been believed that the leading-edge vortex is a convergent aerodynamic solution in the evolution of flight performance in both animals and plants (Lenink *et al.*, 2009; Engels *et al.*, 2016). On the other hand, the autorotating seeds such as those of ash and tulip autorotate while tumbling along their spanwise direction (McCutchen, 1977). As they descend, the leading edge rises and moves back to become the trailing edge continuously. This tumbling motion results from the symmetric chordwise mass distribution unlike the asymmetry of maple seeds (Minami & Azuma, 2003). Therefore, they cannot sustain a stable leading-edge vortex, and thus they descend more rapidly than maple seeds of the same size and weight although they are very stable 1.3. Comprehensive measurements were also performed to study the morphologies of autorotating seeds and their flight performances for many different species (Norberg, 1973; Azuma & Yasuda, 1989; Salcedo *et al.*, 2013; Lee, Lee & Sohn, 2014), and showed a variety of morphological and kinematic characteristics among the species or even for

same species.

1.2 Previous studies on the autorotating seed: theoretical analyses

Some theoretical efforts were conducted to obtain models describing relation among the morphological and kinematical characteristics of autorotating seeds. An autorotating seed is very similar to the wind turbine, and thus some researchers employed mathematical models (momentum theory and blade element theory) that are used to optimize wind turbine blades, in modelling the autorotation phenomenon of seeds (Norberg, 1973; Azuma & Yasuda, 1989; Rosen & Seter, 1991, 1992; Seter & Rosen, 1992; Rao, Hoysall & Gopalan, 2014; Seter & Rosen, 2014). Among others, the axial (linear) momentum theory was introduced to analyze the relation between the geometrical configuration and flight performance of autorotating seeds directly (Norberg, 1973; Azuma & Yasuda, 1989; Rao, Hoysall & Gopalan, 2014). When a seed falls with autorotation, it has terminal descending and rotating velocities, u_T and ω_T, respectively. Using the Galilean transformation with the terminal descending velocity u_T, the seed rotates at the terminal rotating velocity ω_T with zero descending velocity. By ignoring the effect of rotation, Norberg (1973) employed the axial momentum theory and derived a relation of $mg/A_d \propto u_T^2$, where A_d is the disk area, and mg/A_d is the disk loading (m is the mass of the seed, and g is the gravitational acceleration). Subsequently, an optimal model of $u_T = \sqrt{2mg/\rho_f A_d}$ was suggested by (Azuma & Yasuda, 1989) by requiring the axial velocity in far wake u_w to be zero, and provided the minimum rate of descent for disk loading of autorotating seeds. It means that for a given morphological parameters, terminal velocity of a seed cannot be less than that obtained from this limit. These theoretical analyses provided fundamental physics of relation between morphologies

and kinematics of autorotating seeds but are still incomplete. Therefore, it is necessary to adopt some theoretical approaches to capture the nature of autorotating seeds.

1.3 Objectives

As described before, to explore characteristics of autorotating seeds, many experimental and theoretical studies have been conducted, but most of them considered only seeds at the periodic state or in the quiescent condition. Especially, the high-fidelity numerical simulation of autorotating seeds have not been conducted yet due to the complexity of dynamic motions of autorotating seeds. Even it may require the use of grid that continuously adapts in time and that takes into account the new seed orientation and the free stream condition (Rao, Hoysall & Gopalan, 2014). For this purpose, three-dimensional numerical simulations are conducted with a seed model by scanning a maple seed (*Acer palmatum*) using an immersed boundary method in a non-inertial reference frame (Kim & Choi, 2006). Based on the numerical results, improved theoretical models will be suggested to obtain scaling laws describing the relation among the seed weight and geometry, and descending and rotating velocities.

This thesis is organized as follows. In Chapter2, details on the numerical methods for fluid and solid solvers are described. In Chapter 3, the results of flow around a freely-falling maple seed is given and discussed including a experimental validation. In Chapter 4, theoretical analyses are conducted for the relation of morphological and kinematical characteristics of autorotating seeds. Finally, the summary and concluding remarks are followed in Chapter 5.

(*a*)

Maple seed
(by Shutterstock)

(*b*)

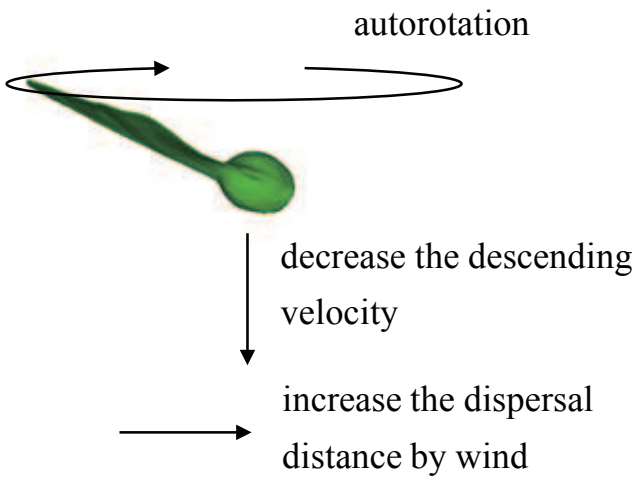

Figure 1.1. (*a*) Maple seed (by Shutterstock); (*b*) schematic diagram of the dispersal mechanism of autorotating seed.

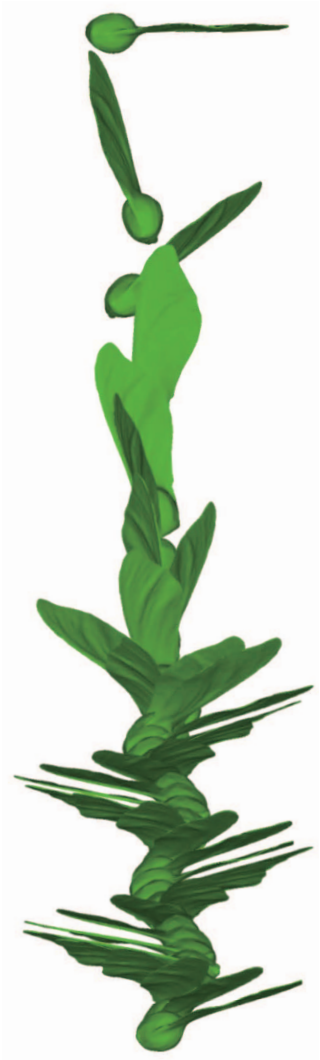

Figure 1.2. Schematic diagram of a free fall trajectories of a single-winged seed.

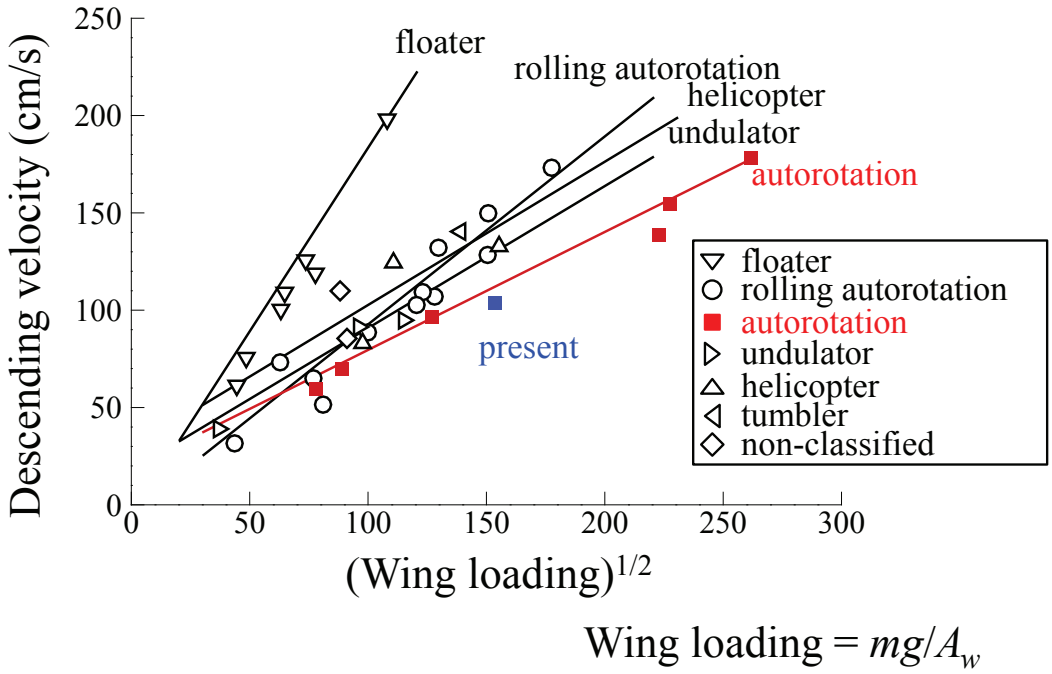

Figure 1.3. Descending time of dispersal seeds including autorotating seeds versus wing loading (Augspurger, 1986).

Chapter 2

Numerical methods

For the present numerical simulation, an immersed boundary method in a non-inertial reference frame fixed to the moving body (seed model in this study) (figure 2.1(a)), which requires much less grid points for resolving fluid motions near the moving body than that in an inertial reference frame (Kweon & Choi, 2010). For incompressible flow, Navier-Stokes and continuity equations are solved. In addition, the Newton and Euler equations are solved for translational and rotational motions of the seed model, respectively. The numerical methods are described in brief here, and the details of numerical methods used are found in Kim & Choi (2006).

2.1 Reference frames

As shown in figure 2.1(a), an inertial reference frame and a non-inertial reference frame fixed to seed model are used. In the inertial reference frame, the translational displacement of body is given as $\boldsymbol{s}_a = (s_x,\, s_y,\, s_z)$. To define the orientation of the moving body, three Euler angles are introduced: $\Theta = (\phi_n,\, \theta_n,\, \psi_n)$. The linear and angular velocities of the body are defined as $\boldsymbol{u}_s = (u_s,\, v_s,\, w_s)$ and $\boldsymbol{\Omega} = (\Omega_x,\, \Omega_y,\, \Omega_z)$, respectively, in the non-inertial reference frame. The Euler angle Θ is used to define a rotation matrix R_m which is written as

$$\mathrm{R}_m = \begin{pmatrix} c\theta_n c\psi_n & -c\phi_n s\psi_n + s\phi_n s\theta_n c\psi_n & s\phi_n s\psi_n + c\phi_n s\theta_n c\psi_n \\ c\theta_n s\psi_n & c\phi_n c\psi_n + s\phi_n s\theta_n s\psi_n & -s\phi_n c\psi_n + c\phi_n s\theta_n s\psi_n \\ -s\theta_n & c\theta_n s\phi_n & c\theta_n c\phi_n \end{pmatrix},$$

where s, c, and t denote the sine, cosine, and tangent, respectively.

The translational velocity of the body with respect to the inertial reference frame, $\dot{\boldsymbol{s}}$, is related to the linear velocity in the non-inertial reference frame using the rotation matrix:

$$\dot{\boldsymbol{s}} = \mathrm{R}_m \boldsymbol{u}_s. \tag{2.1}$$

The angular velocity $\boldsymbol{\Omega}$ in the non-inertial reference frame is related to time time derivative of the Euler angles, and is expressed as

$$\dot{\boldsymbol{\Theta}} = \mathrm{Q}_m \boldsymbol{\Omega}, \tag{2.2}$$

where Q_m is the transformation matrix:

$$\mathrm{Q}_m = \begin{pmatrix} 1 & s\phi_n t\theta_n & c\phi_n t\theta_n \\ 0 & c\phi_n & -s\phi_n \\ 0 & s\phi_n / c\theta_n & c\phi_n / c\theta_n \end{pmatrix}.$$

2.2 Navier-Stokes equations for fluid motion

The governing equations for fluid motion are the unsteady incompressible Navier-Stokes and continuity equations. An immersed boundary (IB) method is used that is defined in a non-inertial reference frame fixed to the moving body proposed by Kim & Choi (2006), in which the no-slip boundary conditions at the moving body surface is satisfied by including momentum forcing and mass source/sink to the Navier-Stokes and continuity equations, respectively:

$$\left(\frac{\partial \boldsymbol{u}}{\partial t}\right)_r + \nabla \cdot [(\boldsymbol{u} - \boldsymbol{v})\,\boldsymbol{u} + \boldsymbol{u}\boldsymbol{w}] = -\nabla p + \frac{1}{Re}\nabla^2 \boldsymbol{u} + \boldsymbol{f}, \tag{2.3}$$

$$\nabla \cdot \boldsymbol{u} - q = 0, \tag{2.4}$$

where $\boldsymbol{u} = \boldsymbol{u}_r + \boldsymbol{v} = \mathrm{R}_m^T \boldsymbol{u}_a$, $\boldsymbol{v} = \boldsymbol{\Omega} \times \boldsymbol{x}_r + \boldsymbol{u}_s$, $\boldsymbol{w} = \boldsymbol{\Omega} \times \boldsymbol{x}_r$, $\boldsymbol{x}_r$ and $\boldsymbol{u}_r$ are the orthogonal coordinates and corresponding velocity vector in the non-inertial reference frame, respectively, p is the pressure, $\boldsymbol{f}$ is the momentum forcing to satisfy the no-slip boundary condition on the IB, q is the mass source/sink to satisfy the mass conservation for the cell containing the IB, $\boldsymbol{\Omega}$ is the angular velocity of the body about the origin of the non-inertial reference frame, R_m is the rotational matrix, R_m^T is the transpose of R_m, and Re is the Reynolds number. In the staggered mesh system, $\boldsymbol{f}$ is applied directly at the grid cell faces, and q is applied at the cell center (figure 2.2). It was shown that the conservative formulation has advantages over the non-conservative one (Kim & Choi, 2006). A fractional-step method is used to solve equations (2.3) and (2.4). In the fractional-step method, a pseudo-pressure is used to correct the velocity vector such that the continuity equation is satisfied at each computational time step. A second-order semi-implicit time advancement scheme is used consisting of a third-order Runge-Kutta (RK3) and the second-order Crank-Nicolson

methods for the convection and diffusion terms, respectively (the overall time accuracy is second order):

$$\begin{aligned}\frac{\hat{\boldsymbol{u}}^k - \boldsymbol{u}^{k-1}}{\Delta t} &= \alpha_k L\left(\hat{\boldsymbol{u}}^k\right) + \alpha_k L\left(\boldsymbol{u}^{k-1}\right) - 2\alpha_k \nabla p^{k-1} - \gamma_k N\left(\boldsymbol{u}^{k-1}\right) \\ &\quad -\rho_k N\left(\boldsymbol{u}^{k-2}\right) + 2\alpha_k \boldsymbol{f}^k, \end{aligned} \tag{2.5}$$

$$\nabla^2 \phi^k = \frac{1}{2\alpha_k \Delta t}\left(\nabla \cdot \hat{\boldsymbol{u}}^k - q^k\right), \tag{2.6}$$

$$\boldsymbol{u}^k = \hat{\boldsymbol{u}}^k - 2\alpha_k \Delta t \nabla \phi^k, \tag{2.7}$$

$$p^k = p^{k-1} + \phi^k - \frac{\alpha_k \Delta t}{Re} \nabla^2 \phi^k, \tag{2.8}$$

where $L(\boldsymbol{u}) = \nabla^2 \boldsymbol{u}/Re$ and $N(\boldsymbol{u}) = \nabla \cdot [(\boldsymbol{u} - \boldsymbol{v})\,\boldsymbol{u} + \boldsymbol{u}\boldsymbol{w}]$. Here, $\hat{\boldsymbol{u}}$ is the intermediate velocity, ϕ is the pseudo pressure, Δt is the computational time step, k is the RK3 substep index ($k = 1,\ 2,\ 3$), and α_k, γ_k, and ρ_k are the coefficients of RK3 substeps ($\alpha_1 = 4/15$, $\gamma_1 = 8/15$, $\rho_1 = 0$; $\alpha_2 = 1/15$, $\gamma_2 = 5/12$, $\rho_2 = -17/60$; $\alpha_3 = 1/6$, $\gamma_3 = 3/4$, $\rho_3 = -5/12$).

The momentum forcing $\boldsymbol{f}^k$ in equation (2.5) is determined in advance such that $\hat{\boldsymbol{u}}^k$ satisfies the no-slip condition on the IB instead of $\boldsymbol{u}^k$, which does not affect the overall second-order temporal accuracy because $\boldsymbol{u}^k = \hat{\boldsymbol{u}}^k - 2\alpha_k \Delta t \nabla \phi^k$ $= \hat{\boldsymbol{u}}^k + O(\Delta t^2)$. To determine $\boldsymbol{f}^k$ near the IB, equation (2.3) is provisionally discretized explicitly in time (RK3 for the convection term and forward Euler method for the diffusion term) only for the fluid cells nearby the IB ($\boldsymbol{f}^k = 0$).

$$\frac{\tilde{\boldsymbol{u}}^k - \boldsymbol{u}^{k-1}}{\Delta t} = 2\alpha_k L\left(\boldsymbol{u}^{k-1}\right) - 2\alpha_k \nabla p^{k-1} - \gamma_k N\left(\boldsymbol{u}^{k-1}\right) - \rho_k N\left(\boldsymbol{u}^{k-2}\right), \tag{2.9}$$

where $\tilde{\boldsymbol{u}}^k$ is the provisional velocity obtained for interpolation purpose. Now,

$\boldsymbol{U}^k$ is the velocity that we want to obtain at a forcing point just inside the IB by applying the momentum forcing. When the forcing point coincides with the IB, $\boldsymbol{U}^k$ is equal to the velocity of the body ($\boldsymbol{v}^k = \boldsymbol{\Omega}^k \times \boldsymbol{x}_r + \boldsymbol{u}_s^k$). However, in general, the forcing points exists inside the body, and thus its value is determined using the linear, bilinear or trilinear interpolation from the velocities $\tilde{\boldsymbol{u}}^k$ (figure 2.3). Then, $\boldsymbol{f}^k$ just inside the IB is obtained as follows (with the same integration method as in equation (2.9)):

$$\begin{aligned} 2\alpha_k \boldsymbol{f}^k &= \frac{\boldsymbol{U}^k - \boldsymbol{u}^{k-1}}{\Delta t} - 2\alpha_k L\left(\boldsymbol{u}^{k-1}\right) + 2\alpha_k \nabla p^{k-1} + \gamma_k N\left(\boldsymbol{u}^{k-1}\right) \\ &\quad + \rho_k N\left(\boldsymbol{u}^{k-2}\right), \end{aligned} \tag{2.10}$$

The details for interpolation scheme for $\boldsymbol{U}^k$ and the procedure of obtaining q^k are described in Kim, Kim & Choi (2001).

2.3 Dynamic equations for the body motion

Three-dimensional motions of a moving body can be described in terms of six components, $\boldsymbol{X} = (\boldsymbol{u}_s, \boldsymbol{\Omega})$, where $\boldsymbol{u}_s$ and $\boldsymbol{\Omega}$ are the translational and rotational velocities of the moving body, respectively. Because the present simulation is fluid-structure interaction problem, the motion of a body is not prescribed but determined by dynamic equations. The Newton and Euler equations for translational and rotational motions in the non-inertial reference frame can be written as

$$m\left[\left(\frac{d\boldsymbol{u}_s}{dt}\right)_r + \boldsymbol{\Omega} \times \boldsymbol{u}_s\right] = \boldsymbol{F}_N + \boldsymbol{F}_e, \tag{2.11}$$

$$\left(\boldsymbol{I}_r \frac{d\boldsymbol{\Omega}}{dt}\right)_r + \boldsymbol{\Omega} \times \boldsymbol{I}_r \boldsymbol{\Omega} = \boldsymbol{T}_N + \boldsymbol{T}_e, \tag{2.12}$$

where m is the mass of the body, $\boldsymbol{I}_r$ is the principal moment of inertia of the body and $\boldsymbol{F}_e$ and $\boldsymbol{T}_e$ are the external force and moment on the body that are not associated with the fluid motion such as the gravitational force. Equations (2.11) and (2.12) are couples with the Navier-Stokes equations because the force $\boldsymbol{F}_N$ and moment $\boldsymbol{T}_N$ acting on the body are determined by the Navier-Stokes equations. Here, $\boldsymbol{F}_N$ and $\boldsymbol{T}_N$ in equations (2.11) and (2.12) are integrated in time using the trapezoidal method in order not to lose the full interaction effect between the fluid and structure, and $\boldsymbol{F}_e$, $\boldsymbol{T}_e$, $\boldsymbol{\Omega} \times \boldsymbol{u}_s$, and $\boldsymbol{\Omega} \times \boldsymbol{I}_r \boldsymbol{\Omega}$ are done using RK3.

$$\begin{aligned} \frac{\boldsymbol{u}_s^k - \boldsymbol{u}_s^{k-1}}{\Delta t} &= \alpha_k \mathrm{M}^{-1} \left(\boldsymbol{F}_N^k + \boldsymbol{F}_N^{k-1}\right) + M^{-1} \left(\gamma_k \boldsymbol{F}_e^{k-1} + \rho_k \boldsymbol{F}_e^{k-2}\right) \\ &\quad -\gamma_k \boldsymbol{\Omega}^{k-1} \times \boldsymbol{u}_s^{k-1} - \rho_k \boldsymbol{\Omega}^{k-2} \times \boldsymbol{u}_s^{k-2}, \end{aligned} \tag{2.13}$$

$$\begin{aligned} \frac{\boldsymbol{\Omega}^k - \boldsymbol{\Omega}^{k-1}}{\Delta t} &= \alpha_k \boldsymbol{I}_r^{-1} \left(\boldsymbol{T}_N^k + \boldsymbol{T}_N^{k-1}\right) + \boldsymbol{I}_r^{-1} \left(\gamma_k \boldsymbol{T}_e^{k-1} + \rho_k \boldsymbol{T}_e^{k-2}\right) \\ &\quad -\boldsymbol{I}_r^{-1} \left(\gamma_k \boldsymbol{\Omega}^{k-1} \times \boldsymbol{I}_r \boldsymbol{\Omega}^{k-1} + \rho_k \boldsymbol{\Omega}^{k-2} \times \boldsymbol{I}_r \boldsymbol{\Omega}^{k-2}\right). \end{aligned} \tag{2.14}$$

Here, the non-dimensional force $\boldsymbol{F}_N$ and moment $\boldsymbol{T}_N$ exerted on a body by fluid in the non-inertial reference frame are evaluated as

$$\boldsymbol{F}_N^k = -\left[\int_V \boldsymbol{f}^k \, \mathrm{d}V - V\left(\frac{\boldsymbol{u}_s^k - \boldsymbol{u}_s^{k-1}}{2\alpha_k \Delta t} + \boldsymbol{\Omega}^{k-1} \times \boldsymbol{u}_s^{k-1}\right)\right], \tag{2.15}$$

$$\boldsymbol{T}_N^k = -\left(\int_V \boldsymbol{x}_r \times \boldsymbol{f}^k \, \mathrm{d}V - \boldsymbol{I}_r \frac{\boldsymbol{\Omega}^k - \boldsymbol{\Omega}^{k-1}}{2\alpha_k \Delta t}\right), \tag{2.16}$$

where V is the volume of the body. Note that the second terms in the right-hand

sides of equations (2.15) and (2.16) corresponds to the inertial and moment of the body, respectively. These force and moment can be easily converted into those ($\boldsymbol{F}_I$ and $\boldsymbol{T}_I$) in the inertial reference frame by multiplying the rotational matrix R_m:

$$\boldsymbol{F}_I^k = \mathrm{R}_m^k \boldsymbol{F}_N^k, \tag{2.17}$$

$$\boldsymbol{T}_I^k = \mathrm{R}_m^k \boldsymbol{T}_N^k. \tag{2.18}$$

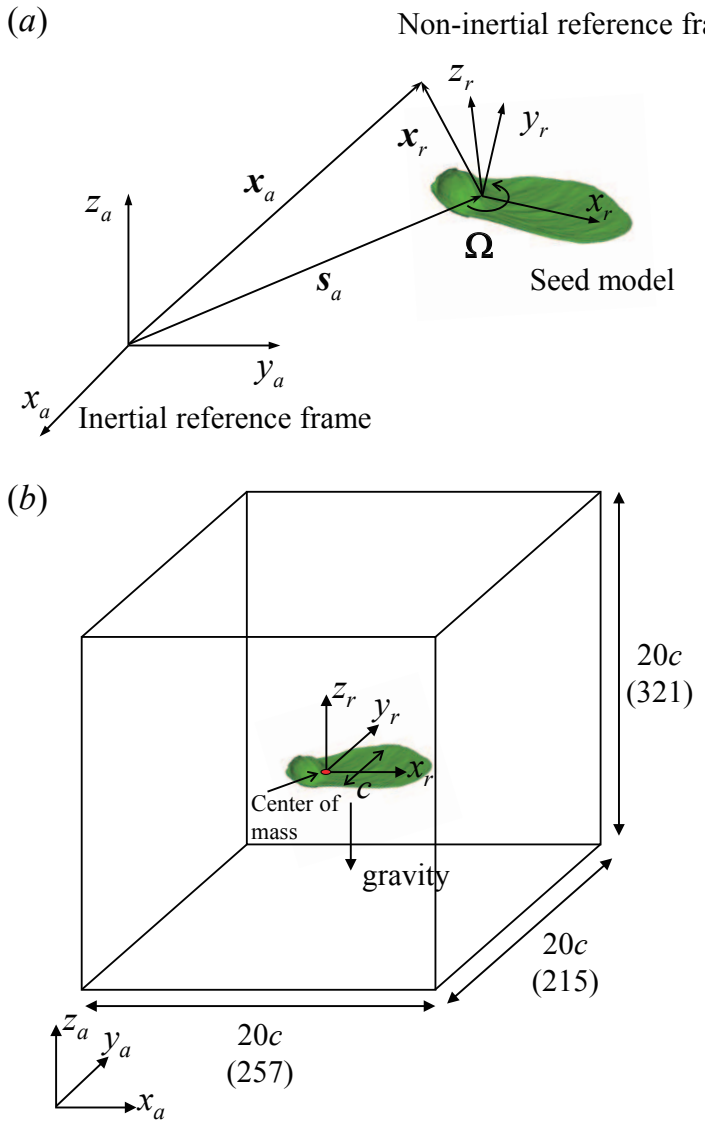

Figure 2.1. (a) Schematic diagram of the seed model and coordinate systems, (x_a, y_a, z_a) in an inertial reference frame and (x_r, y_r, z_r) in a non-inertial reference frame fixed to the seed model; (b) schematic diagram of the computational domain and corresponding number of grid points with initial posture of the seed model.

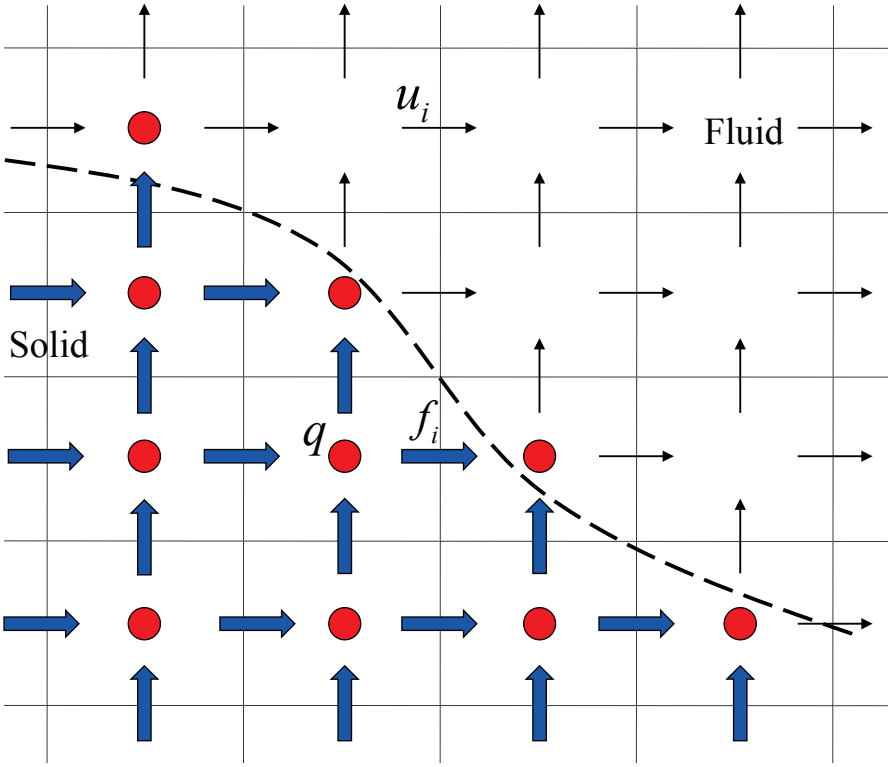

Figure 2.2. Schematic diagram of locations of the momentum forcing and mass source/sink. The solid and dashed lines denote the grid lines and IB, respectively.

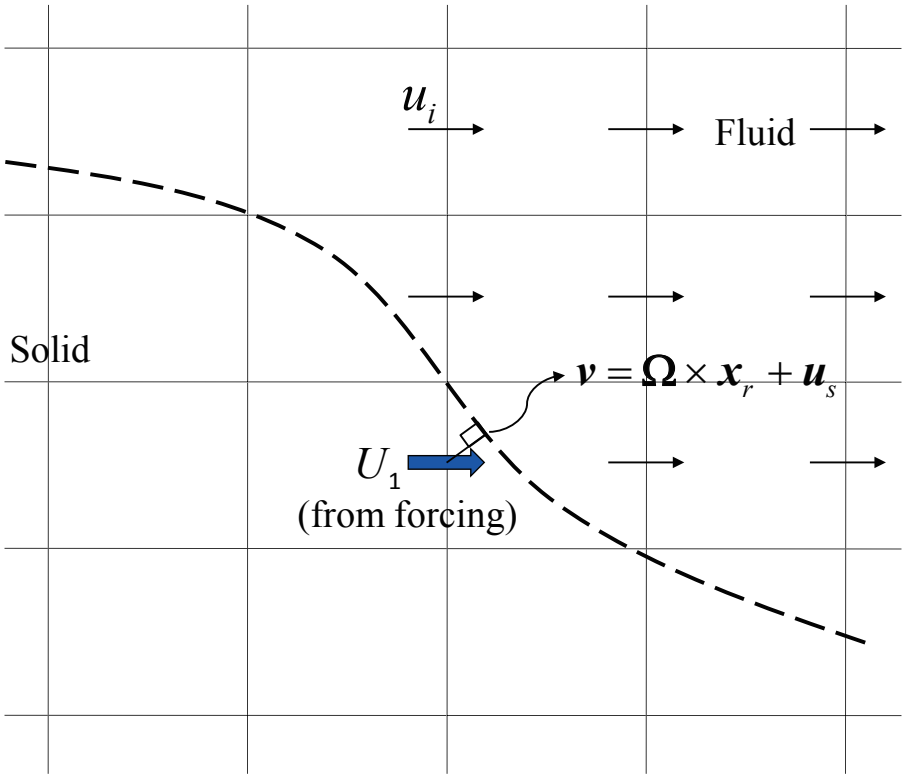

Figure 2.3. Schematic diagram of the bilinear interpolation scheme.

Chapter 3

Characteristics of a freely-falling maple seed

Three dimensional numerical simulations are conducted to investigate the characteristics of a freely-falling maple seed in the quiescent condition. The seed falls with rotating motion and its descending velocity decreases rapidly after a transient period. Then the seed reaches the periodic state with its terminal descending and rotating velocities. With the same maple seed, free-fall test is conducted to obtain its terminal descending and rotating velocities for a validation. The measured terminal velocities are in good agreement with those of high-fidelity numerical simulation indicating the accuracy of the present study. At the periodic state, due to the rotating wing motion, the leading-edge, trailing-edge, wing-tip, and wing-root vortices are generated as similar to those of hovering insect wing. Especially, the leading-edge vortex remains stable along the wing surface rather than sheds into the wake, which is known to create high drag force. The portion of drag force acting on the wing (center of mass to wing tip) is about 9 times greater than that on the nut (base to center of mass) indicating the leading edge vortex on the rotating wing play a prominent role in generating the drag force. The effect of the initial posture on the entrance into autorotation is studied. For this purpose, leading-edge upward, trailing-edge upward, nut upward, and wing-tip upward cases are also simulated in addition to the wing-surface upward case. The autorotation occurs earlier when the leading-edge or nut is initially positioned upward. This indicates that the

natural initial posture may be for fast entrance into autorotation. The effect of the presence of the wind is also studied by increasing the free-stream velocities. With increasing the magnitude of the wind velocity, the flying velocities of the freely-falling maple seed increases and reaches at almost same values of the wind velocities. As similar to those of freely-falling maple seed in the quiescent condition, initially the descending velocity increases almost linearly, and then decreases as the rotating velocity increases. Then the seed reaches a periodic state with terminal descending and rotating velocities maintaining the leading-edge vortex on the wing surface regardless of the presence of wind.

3.1 Experimental validation

First, free-fall experiment is conducted with a maple seed for the purpose of validation of the present numerical simulation. The seed used in this experiment is (*Acer palmatum*), which is one of the most prevailing species of maples in Korea (Lee & Lee, 2016). Figure 3.1(a) shows the schematic diagram of experimental setup and arrangements of the apparatus for this free-fall test. To measure the descending and rotating motions of maple seed, two high-speed cameras and two 2 kW-Tungsten portable lights as an illumination source are used in a customized studio frame (2.0 m $\times$ 2.0 m $\times$ 2.0 m) that is covered with blackout curtains to avoid external disturbances during the experiments (Lee, Park & Kim, 2015). Two high-speed cameras, one located on the top and other capturing side view, are operated simultaneously via a synchronizer. The image capturing was done for 2 seconds at the rate of 1000 fps, which is sufficient to resolve both the descending and rotating motions of the seed (Varshney, Chang & Wang, 2012), with a spatial resolution of 512 $\times$ 512 pixels. To calibrate the cameras, an in-house calibration target is used (figure 3.1(b)), and it has

100 circular dots distributed with a spacing of 40 mm in lateral and vertical directions as done in Lee, Park & Kim (2015). The maple seed is released from 2.0 m above the floor of the studio frame, which is enough to reach the steady autorotation. The detailed experimental setup is in Lee, Park & Kim (2015).

To measure the descending and rotating velocities of the seed, a visual image correlation method is used (Hedrick, 2008). The descending velocity can be calculated from falling distance evaluated between two images divided by the time interval between them, 109.3 mm descent during 0.112 s. Also the rotating velocity is obtained from the time elapsed during five revolution by counting number of frames between the two images, 18.858 rad rotation during 0.112 s. Then, the measured terminal descending and rotating velocities are u_T = 0.976 m/s and ω_T = 168.4 rad/s, respectively. To verify the measured terminal velocities, a rough measurement are also conducted. Figures 3.2 and 3.3 show the top- and side-view images for descending and rotating motions of the seed, respectively. As similar to the study on Lee, Lee & Sohn (2014), the descending velocity is checked by comparing with a vertically mounted reference scale. In figure 3.2, the elapsed time between the first and second images is 0.18 s and the corresponding descending distance is about 170 mm. From this, a roughly measured descending velocity is about 0.944 m/s which is very similar to that from image correlation method. Also, a roughly measured rotating velocity is about 169.8 rad/s (37 frames during one revolution) confirming the measured data from image correlation method. Non-dimensional values of measured velocity components of u_T = 0.976 m/s and ω_T = 168.4 rad/s are $U_T(u_T/u_g)$ = 0.237 and $\Omega_T(c\omega_T/u_g)$ = 0.175, respectively, and they will be compared with those of high-fidelity numerical simulation.

3.2 Computational details

For the numerical simulation, a three-dimensional seed model is obtained by scanning the maple seed and its geometrical configuration is shown in figure 3.4. Here, the wing (blade) of seed is assumed as rigid body because the deformation of the wing is negligible. The scanned model provides surface meshes of the seed that are used to identify the grid points for momentum forcing as described in the previous section of numerical methods (section 2.2). As shown in figure 3.4(a), the seed has numerous vascular bundles that spread out toward the wing-tip of the seed, and thick vascular bundles are concentrated near the leading edge of the seed (Lee, Lee & Sohn, 2014). The mass distribution of the seed is obtained by varying the thickness of the wing, which is thickest at the leading edge and becomes thin towards the trailing edge (Norberg, 1973). Therefore, it can be assumed that the mass distribution on the seed is directly related to the thickness variation, and one can obtain the location of the center of mass which is same location with center of rotation (figure 3.4(b)).

The dimensionless morphological parameters of the seed are $\rho = 405$, $V = 0.304$, and $(I_{xr},\ I_{yr},\ I_{zr}) = (7.7,\ 70.5,\ 73.8)$, where ρ $(=\rho_s/\rho_f)$ is the ratio of seed to fluid densities, V and I_{ir} are the seed volume and principal moments of inertia normalized by c^3 and $\rho_f c^5$, respectively, c (A_w/R_w) is the mean chord length, and A_w and R_w are the wing planform area (from the center of mass to wing tip) and wing span of the seed, respectively. The aspect ratio of the wing is AR $(R_w^2/A_w) = 2.62$ (low aspect ratio wing) which is similar to those of insect wings (Kweon & Choi, 2010).

The computational domain size is $-10c \leq x_r \leq 10c$, $-10c \leq y_r \leq 10c$, $-10c \leq z_r \leq 10c$, and the number of grid points is $257 \times 215 \times 321$ in x_r, y_r, z_r directions, respectively. The origin of the moving coordinates coincides

ρ	V	I_{xr}	I_{yr}	I_{zr}	Re	Fr
405	0.304	7.7	70.5	73.8	1171	20.1

Table 3.1. Morphological and computational parameters for a maple seed (*Acer palmatum*)

with the center of mass of the seed model. The Neumann boundary conditions ($\partial \boldsymbol{u}/\partial \boldsymbol{n}$) are used at whole boundaries, where $\boldsymbol{n}$ is the vector normal to the outer boundary surface. The Reynolds and Froude numbers corresponding to the seed model are $Re = u_g c/\nu = 1171$ and $Fr = u_g/\sqrt{cg} = 20.1$, respectively, where ν is the kinematic viscosity, u_g $(= \sqrt{(\rho - 1)cg})$ is the characteristics velocity, and g is the gravitational acceleration. Computations are performed at the maximum CFL number of 0.6.

3.3 Kinematic characteristics

As shown in the schematic diagram of the computational domain in previous chapter (figure 2.1(b)), the initial posture of the seed is the wing surface upward with respect to the direction of the gravitational force, and then the seed freely falls without any disturbance in the quiescent flow condition. Figure 3.5 shows the trajectories of the center of mass and wing tip of the freely-falling seed model. The seed falls almost vertically in spite of its very long descending vertical distance (dotted red line in figure 3.5(a)). The wing tip shows a helical path, and the center of mass also shows a rotating motion but with a much larger period. Figure 3.6(a)) shows the projected falling trajectories of center of mass and wing tip, and figure 3.6(b)) shows the time trace of horizontal velocity of center of mass. As shown, both high and low frequency components

of center of mass are observed from the horizontal velocity. As a result, the characteristic frequencies of center of mass are can be obtained as shown in figure 3.7). Here, the high frequency of center of mass is same as that of wing tip. Figure 3.8 shows the time traces of the velocity components in the inertial reference frame and their corresponding translational displacements. As shown, the lateral motions (dashed and dash-dot lines) are small in comparison with descending motion (solid blue line). Generally, it can be defined that the seed enters into autorotation when the radius of rotation from the center of mass reaches almost constant value meaning stable rotation. After a transient period, the radius of rotation reaches a periodic state at $tu_g/c \backsim 400$ at which the descending vertical distance is $z_a/c = 159$ (0.68 m in dimension). It was known that maple seeds typically reach periodic autorotation within 1 m of detaching from the tree (Lenink *et al.*, 2009), and the present result is also in agreement with the previous observation.

Figure 3.10 shows the time traces of the drag coefficient ($D/\rho_f u_T^2 A_d$), descending (u_d/u_g) and rotating ($c\omega_d/u_g$) velocities, where D is the drag defined as the force component acting on the opposite direction of gravity (vertical force), A_d ($= \pi {R_d}^2/c^2$) is the disk area, and R_d is the radius of rotation from the center of mass at periodic state. At a certain rotation rate, the outward centrifugal force of the rotation balances the upward and inward tilt due to the drag, and the seed adopts an equilibrium coning angle (Alexander & Vogel, 2003). Therefore, note also that the disk radius R_d is not exactly same as that of the wing span R_w because descending seeds have a coning angle about $13^\circ \sim 17^\circ$ (Azuma & Yasuda, 1989). Time trace of the coning angle is shown in figure 3.11. It shows that the coning angle fluctuates in time, and gives the time-averaged coning angle of $\beta = 11^\circ$ which is very similar to those of previous measured data (Azuma & Yasuda, 1989). As shown in figure 3.10(b), initially

the descending velocity increases almost linearly, and then decreases as the rotating velocity increases, where the rotational direction is counter-clockwise. Later, the seed model reaches a periodic state with terminal descending and rotating velocities whose non-dimensional time-averaged values are $U_T = 0.252$ and $\Omega_T = 0.165$ ($U_T = 0.237$ and $\Omega_T = 0.175$ from measured data in free-fall test). At this state, the time-averaged drag coefficient is $C_{D,T} = 0.457$. The present numerical results show only 6.33% and 5.71% differences from the experimental results of terminal descending and rotating velocities, respectively, indicating the accuracy of the present study. As the seed rotates, it maintains pitching angle in a certain range as shown in figure 3.12(b). It was known that a positive slope of pithing moment curve is necessary for the stability (Park & Choi, 2010), and this phenomenon is also shown in this study (figure 3.12(c)).

So far, the present simulation shows the descending motion with counter-clockwise rotation. However, it was observed that the autorotating seeds have no specific rotating direction, but they rotate either in the clockwise or counter-clockwise direction (Alexander & Vogel, 2003; Varshney, Chang & Wang, 2012). To confirm this phenomenon, another simulation is conducted with the same seed model while the opposite side of the wing surface is positioned upward, and it shows the falling motion with clockwise rotation. Figure 3.13 shows the time traces of the descending and rotating velocities for the cases with two different rotating directions. As shown, the falling seed with counter-clockwise rotation has lower terminal descending and faster terminal rotating velocities than those of the falling seed with clockwise rotation.

3.4 Flow characteristics

In this section, the flow structures around the freely-falling maple seed are investigated. Figure 3.14 shows the instantaneous three-dimensional vortical structure around the seed model at four different time instants (transient states (a, b) and periodic states (c, d)), identified by the isosurface of λ_2 = -0.1 (Jeong & Hussain, 1995). At early stages of the free fall, the seed descend like gliding wing or falling rock, and the vortical structures generated are shed into the wake because the seed only descend without rotating motion (figures 3.14(a) and (b)). On the other hand, in the periodic state (figure 3.14(c) and (d)), due to the rotating and descending motion, the leading-edge, trailing-edge, wing-tip, and wing-root vortices are generated (figure 3.15) as similar to those of hovering insect wing (Kweon & Choi, 2010). The wing-tip vortex exists as a helical shape along the wing-tip trajectory as seen in the wake behind wind turbines. As shown, especially the leading-edge vortex remains stable along the span rather than sheds into the wake, which creates high drag force (Lenink *et al.*, 2009; Salcedo *et al.*, 2013; Lee, Lee & Sohn, 2014). Figure 3.16 shows the instantaneous pressure contours around spanwise sections of rotating wing. The leading-edge vortex ensures low-pressure regions on the upper surface of rotating wing, which enhances the drag (figure 3.16). It has been believed that the leading-edge vortex is a convergent aerodynamic solution in the evolution of flight performance solution in the evolution of flight performance in both animals and plants (Lenink *et al.*, 2009; Engels *et al.*, 2016).

Figure 3.17 shows the contours of instantaneous spanwise vorticity at four different planes at r/R_d = 0.2, 0.4, 0.6 and 0.8. The leading-edge vortex is most prominent near the base (nut) of the maple seed, shown at r/R_d = 0.2, but it merges with the tip vortex near the wing tip (r/R_d = 0.8), resulting in

a long trail of vorticity in the wake (Lenink *et al.*, 2009). (Lenink *et al.*, 2009) found that autorotating seeds generate a prominent leading-edge vortex near the base and the leading-edge vortex is more compact at lower angles of attack from experiments using a dynamically scaled model. The stable attachment of the leading-edge vortex is thought partly on strong spanwise flow on the wing surface that drains vorticity from leading-edge vortex toward the wing-tip vortex (Ellington *et al.*, 1996; Birch & Dickinson, 2001), and this process stretches and tightens the leading-edge vortex. Therefore it prevents the leading-edge vortex from growing so large that it becomes unstable and sheds into the wake (Lenink *et al.*, 2009). This strong spanwise flows on the wing surface of the seed are also observed in this study (figure 3.18).

3.5 Sectional drag coefficient

To investigate the three-dimensional flow characteristics around the rotating wing, it is effective to compare the sectional drag and the vortical structures around the wing section simultaneously (Kweon, 2011). The investigation of sectional drag coefficient provides helpful data to analytically estimate the drag forces generated on the insect wing, blade element method (Sane & Dickinson, 2001). The blade element theory was originally developed to obtain the forces and moments on a rotating propeller or rotor by breaking down a wing (or blade) into several elements, determining the sectional drag force on each wing element, and integrating them along the entire wing. One of the important components for the blade element theory is to know the radial distribution of the sectional drag coefficient. In this study, to further understand the flow characteristics around the autorotating seed, the sectional drag force coefficient is also investigated.

The sectional drag coefficient on each wing element (Δr) can be defined as

$$C_{D,S}(r) = \frac{2\Delta F_D(r)}{\rho_f U(r)^2 c(r) \Delta r}, \tag{3.1}$$

where $\Delta F_D(r)$ is the sectional drag force, r is the spanwise direction, $c(r)$ is the chord length at each element, Δr is the section length at each element, and $U(r)$ $(= \sqrt{(r\omega_T)^2 + u_T^2})$ is the reference velocity at each wing element, respectively. Note that the $U(r)$ defined in this study is different from previous one used in the study of hovering insects wing (Kweon & Choi, 2010) due to the descending velocity of autorotating seeds as well as rotating velocity: only the rotating velocity in hovering insects wing.

Usually, the sectional drag coefficient is assumed to be constant in the radial direction based on the potential theory for the rotating wing with a high aspect ratio at high Reynolds number. This assumption is also valid even for the wing with an intermediate aspect ratio (Morino *et al.*, 1989). However, for the rotating wing with low-aspect ratio wings in rotating motion, the sectional drag coefficient is proportional to $1/r$ along the span except near the wing tip (Kweon & Choi, 2010). Here, the similar approach is also conducted to investigate the characteristics of sectional drag coefficient of autorotation seeds. Figure 3.19 shows the spanwise distribution of period-averaged sectional drag coefficient of the autorotating seed at periodic state (solid line with black square). As shown, the sectional drag coefficient decreases in spanwise direction for the wing section. Most wing-sections of maple seed has high angles of attack in the range of $30^\circ \sim 60^\circ$, and their distributions are quite similar to those of revolving fruit fly and rectangular wings at high angles of attack (Kim, Kweon & Choi, 2015). Here, the sectional drag coefficient defined as $2\Delta F_L(r)/\rho_f u_T^2 c \Delta r$, normalized by terminal descending velocity and mean chord length at each radial direction, is

also plotted for the direct comparison of magnitude of the sectional drag force (solid line with hollow square). As shown in this figure, the sectional drag force reaches maximum value near 60% span of the wing. By integrating the sectional drag force, it can be found that the portion of drag force acting on the wing (center of mass to wing tip) is about 9 times greater than that on the nut (base to center of mass), i.e. 90% of total drag force , and this indicates the stable leading-edge vortex on the rotating wing play a prominent role in generating the high drag force. The sectional drag coefficient obtained are used in the next chapter for scaling law to elucidate the relation between the morphological and kinematical characteristics of autorotating seeds.

3.6 Initial posture of the seed

In nature, many winged seeds are attached to the plant with certain posture, long axis near to horozontal or the nut (center of mass) upward initially (figure 1.1(a)). On the other hand, when a seed is falls with its wing-tip directed strictly upward (i.e. center of mass downward), it usually needs a high fall before entrance into autorotation, or fails to rotate at all (Norberg, 1973). Based on this observation study, the effect of the initial posture of the seed on the autorotation is investigated with same seed model. For this purpose, four initial postures are simulated in addition to previous two different wing-surface upward cases: initially leading-edge upward, nut upward, trailing-edge upward and wing-tip upward cases as depicted in figure 3.20. Depending on the initial posture of the seed, different transitional processes occur before the periodic state (Lee & Lee, 2016). Figure 3.21 shows the time traces of the descending and rotating velocities for the cases of different initial postures, and figure 3.22 shows the time period for only transient region to investigate more detail

about the effect of different initial postures on the entrance into autorotation. As mentioned before, once centrifugal forces act through the wing, the seed rapidly reaches autorotation in common for all cases and adjusts its attitude to the inherent sectional angle of attack and coning angle regardless of its initial posture. However, as shown in the time trace of descending velocity, the transient periods from leading-edge and nut-upward cases are shorter than that of wing-tip upward case. Also in the case of rotating velocity, these two cases reach faster rotating velocity earlier than wing-tip upward case. Note that the seed also enters into the autorotation even in the case of wing-tip upward rather than fails to autorotation. Because the wing of the seed is somewhat bent, twisted, or its trailing edge undulated rather than smooth, lateral aerodynamic forces on the irregular surface of wing may induce a circular path of the wing tip, whereby centrifugal forces are set up (Norberg, 1973). The slight differences of values for terminal descending and rotating velocities are from different rotational directions (clockwise and counter-clockwise directions) as described in previous section 3.3. The time traces of the radius of rotation from center of mass is shown in figure 3.23) for more apparent comparison of the time to reach autorotation for different initial postures. In section 3.3, it was defined that the seed enters into autorotation when the radius of rotation reaches almost constant value ($R_d/c = 2.57$). As shown in this figure, the radius of rotation reaches at periodic state more rapidly in the cases of leading-edge upward and nut upward than that of wing-tip upward. Therefore, it means that the autorotation occurs earlier when the leading-edge or nut is initially positioned upward than when the wing tip is positioned upward, and thus the natural initial posture of the seeds (leading-edge or nut upward) may be for fast entrance into autorotation.

3.7 Freely-falling maple seed in the presence of wind

Previous researches were conducted with the situation of freely-falling seeds in the quiescent condition. However, in real situation, the freely-falling seeds are dispersed by wind, and thus the presence of the wind should be considered. Figure 3.24 shows the schematic diagram of the computational domain for the simulation of the freely-falling maple seed in the presence of wind. To investigate the characteristics of autorotating seed in the presence of wind, the simulation is conducted at the same conditions except the boundary condition. In the case of the autorotating seed in the quiescent condition, the Neumann boundary conditions ($\partial u_i/\partial n_j$) are used at whole boundaries, where n_j is the vector normal to the outer boundary surface. On the other hand, the Dirichlet and Neumann boundary conditions are used for the simulations of flow around a freely-falling maple seed in the presence of wind. The details about boundary conditions are $u = \mathrm{R}_m^T(1,j)\boldsymbol{u}_\infty$, $\partial v/\partial n = 0$ and $\partial w/\partial n = 0$ at x_r = -10, $\partial \boldsymbol{u}/\partial n = 0$ at $x_r = 10$, $u = \partial u/\partial n$, $v = \mathrm{R}_m^T(2,j)\boldsymbol{u}_\infty$ and $\partial w/\partial n = 0$ at y_r = -10, $\partial \boldsymbol{u}/\partial n = 0$ at $y_r = 10$, $u = \partial u/\partial n$, $\partial v/\partial n = 0$ and $w = \mathrm{R}_m^T(3,j)\boldsymbol{u}_\infty$ at $z_r = -10$, and $\partial \boldsymbol{u}/\partial n = 0$ at $z_r = 10$, respectively (figure 3.24), where $\boldsymbol{u} = (u_w/u_T, 0, 0)$ and u_w is the velocity of wind. Here, Dirichlet boundary conditions change in time due to the rotational matrix R_m for the transformation of information in non-inertial reference frame into inertial reference frame or vice versa, and R_m is defined in chapter 2. Computations are performed at the maximum CFL number of 0.5.

The initial posture of the seed is selected as close to the natural initial posture, the leading-edge upward with respect to the direction of the gravitational acceleration (figure 3.20). Figure 3.25(a) shows the time traces of the flying velocity (same direction with wind velocity) of the freely-falling seed. As

shown, with increasing the magnitude of the wind velocity, the flying velocities of the seed increase and reach at almost same values of the wind velocities. Figure 3.25(b) shows the time traces of the descending and rotating velocities of the freely-falling maple seed in the presence of the wind. As similar to those of freely-falling maple seed in the quiescent condition, initially the descending velocity increases almost linearly, and then decreases as the rotating velocity increases. Later, the seed model reaches a periodic state with terminal descending and rotating velocities like the freely-falling seed in the quiescent condition. However, the seed reaches larger maximum descending velocity in the presence of the wind than in the quiescent condition. Time trace of the horizontal radius of rotation from the center of mass is shown in figure 3.26. As shown in this figure, the radius of rotation reaches at periodic state more rapidly in the case of quiescent condition than in the presence of the wind. Figure 3.27 shows the instantaneous three-dimensional vortical structures around the seed model, and the leading-edge vortex also remains stable along the span rather than sheds into the wake and creates high drag force for all cases considered. Therefore, for the wind velocities considered in this study, this result means that the autorotating seed retain its inherent characteristics of stable leading edge vortex on the wing regardless of the presence of wind.

3.8 Summary

In this chapter, three dimensional numerical simulations were conducted for flows around a freely-falling maple seed in the quiescent condition. After a transient period, the seed rotated as a helical shape and its descending velocity decreases rapidly. Then the seed reached the periodic state with its terminal descending and rotating velocities. In addition, a free-fall test was conducted

to obtain its terminal descending and rotating velocities for the verification of the present numerical simulation. The measured terminal descending and rotating velocities were in good agreement with those of high-fidelity numerical simulation indicating the accuracy of the present study. The seed descended with a periodic rotating motion with almost constant radius of rotation from the center of mass, $R_d/c = 2.57$ and corresponding time to reach a periodic autorotation was about $tu_g/c = 400$ at which the descending vertical distance is $z_a/c = 159$ (0.68 m in dimension). It was known that maple seeds typically reach periodic autorotation within 1 m of detaching from the tree (Lenink *et al.*, 2009), and the present result was also in agreement with the previous observation. At the periodic state, due to the rotating wing motion, the leading-edge, trailing-edge, wing-tip, and wing-root vortices were generated as similar to those of hovering insect wing. Especially, the leading-edge vortex remained stable along the span of the wing rather than sheds into the wake, which is known to create high drag force. From the spanwise vorticity contours, the leading-edge vortex was most prominent near the base (nut) of the maple seed, but it merged with the tip vortex near the wing tip, resulting in a long trail of vorticity in the wake, and the strong spanwise flows on the wing surface of the seed were also observed.

To further understand the flow characteristics around the autorotating seed, the sectional drag coefficient was also investigated. By integrating the sectional drag force, it was found that the portion of drag force acting on the wing (center of mass to wing tip) is about 9 times greater than that on the nut (base to center of mass) indicating the leading-edge vortex on the rotating wing play a prominent role in generating the high drag force. The effect of the initial posture on the entrance into autorotation was also studied. For this purpose, leading-edge upward, trailing-edge upward, nut upward, and wing-tip upward cases were

also simulated in addition to the wing-surface upward case. The autorotation occurred earlier when the leading-edge or nut was initially positioned upward than when the wing tip was positioned upward, indicating that the natural initial posture of the seed is effective for fast entrance into autorotation and also for the conservation of species. The effect of the presence of the wind was studied by increasing the free-stream velocities. With increasing the magnitude of the wind velocity, the flying velocities of the freely-falling maple seed increased and reached at almost same values of the wind velocities. As similar to those of freely-falling maple seed in the quiescent condition, initially the descending velocity increased almost linearly, and then decreased as the rotating velocity increased. Then the seed reached a periodic state with terminal descending and rotating velocities maintaining the leading-edge vortex on the wing surface regardless of the presence of wind.

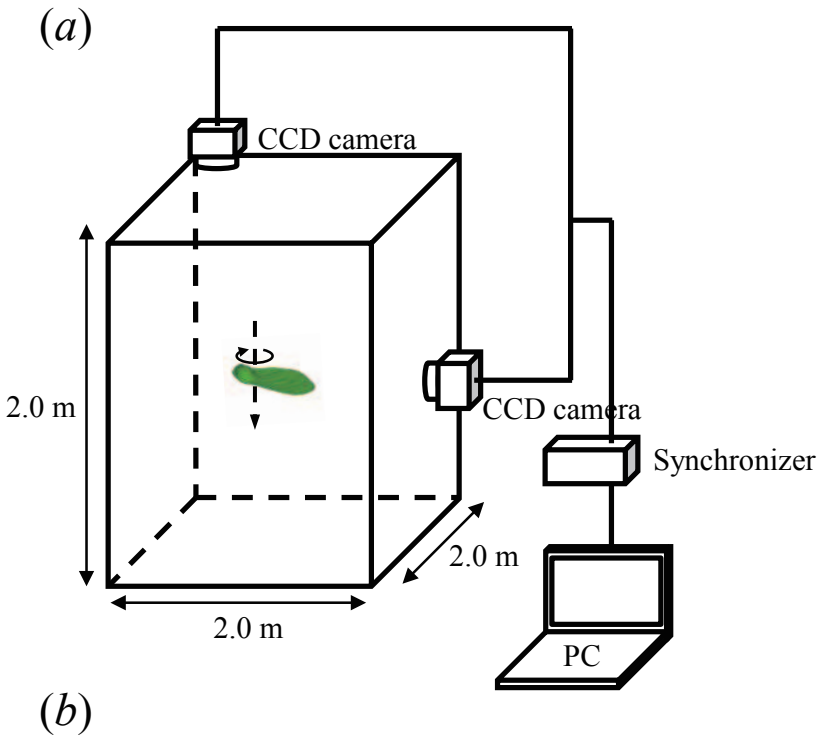

Figure 3.1. (a) Schematic diagram of experimental setup for a free-fall test; (b) calibration target with one hundred markers (Lee, Park & Kim, 2015).

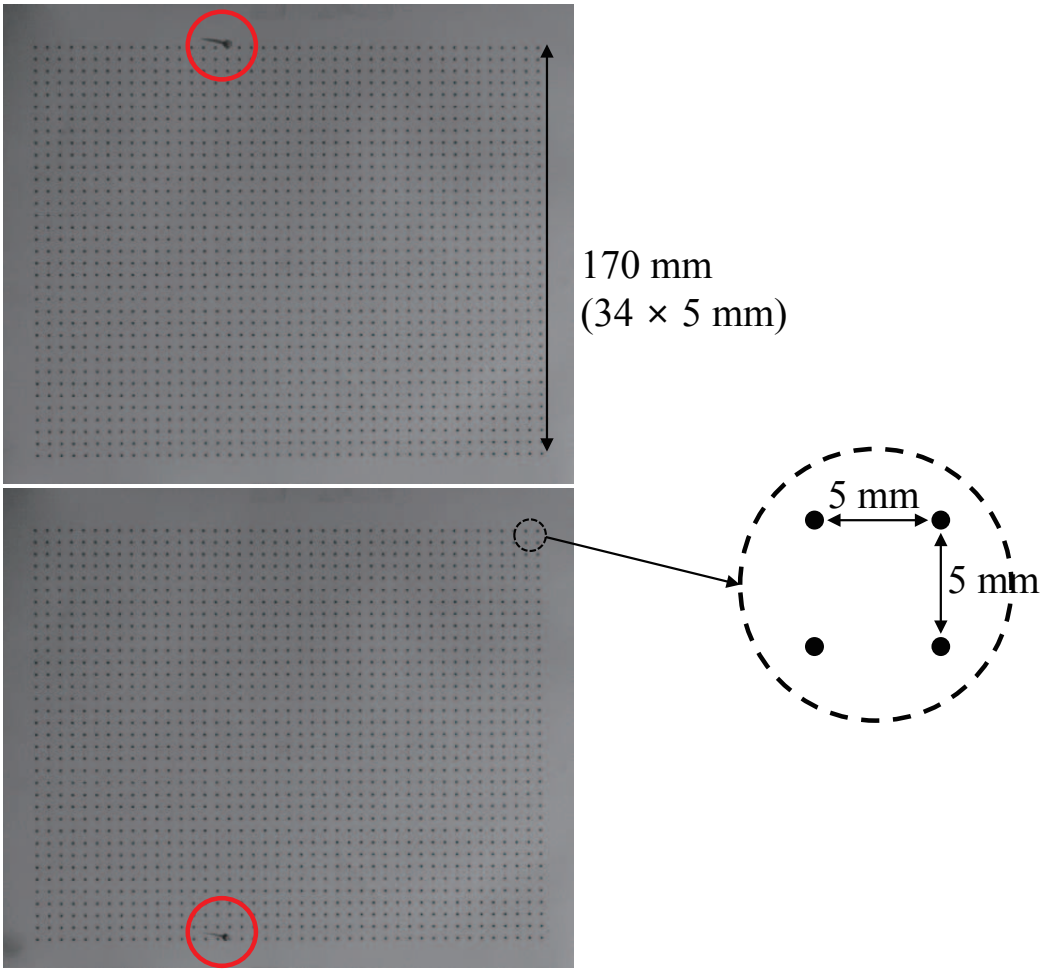

Figure 3.2. Side-view images for descending motion of the seed during 0.18 sec.

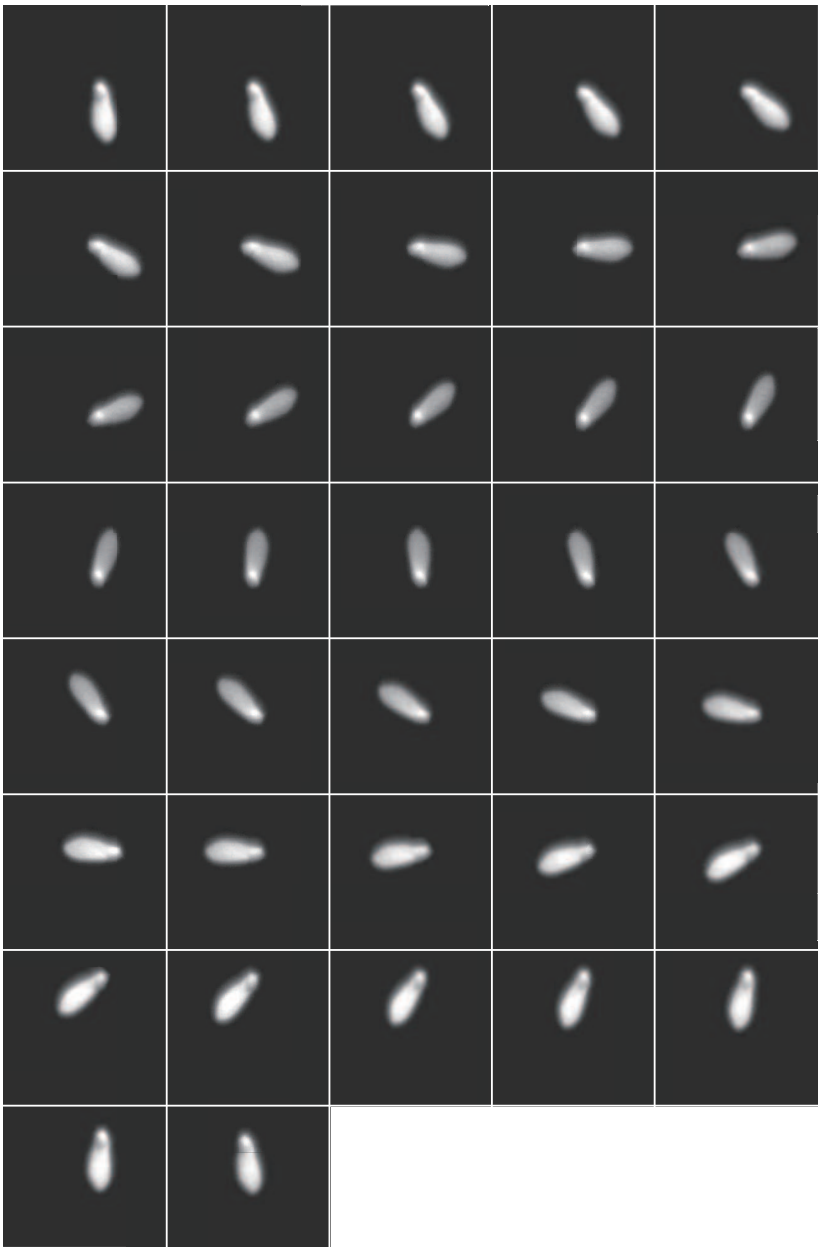

Figure 3.3. Top-view images for rotating motions of the seed during 0.037 sec.

(*a*)

(*b*)

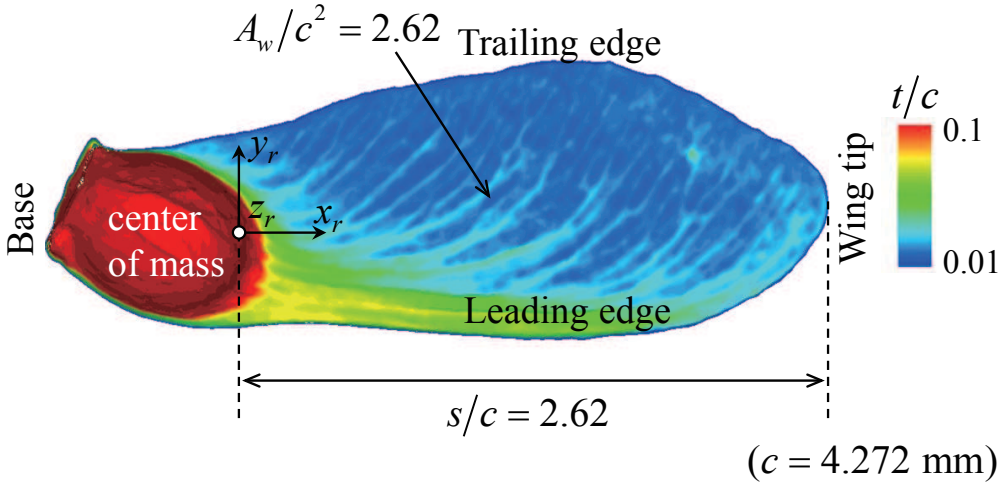

Figure 3.4. (*a*) Maple seed (*Acer palmatum*); (*a*) scanned three-dimensional seed model. In (*b*), colors indicate the non-dimensional thickness (t/c) of the seed.

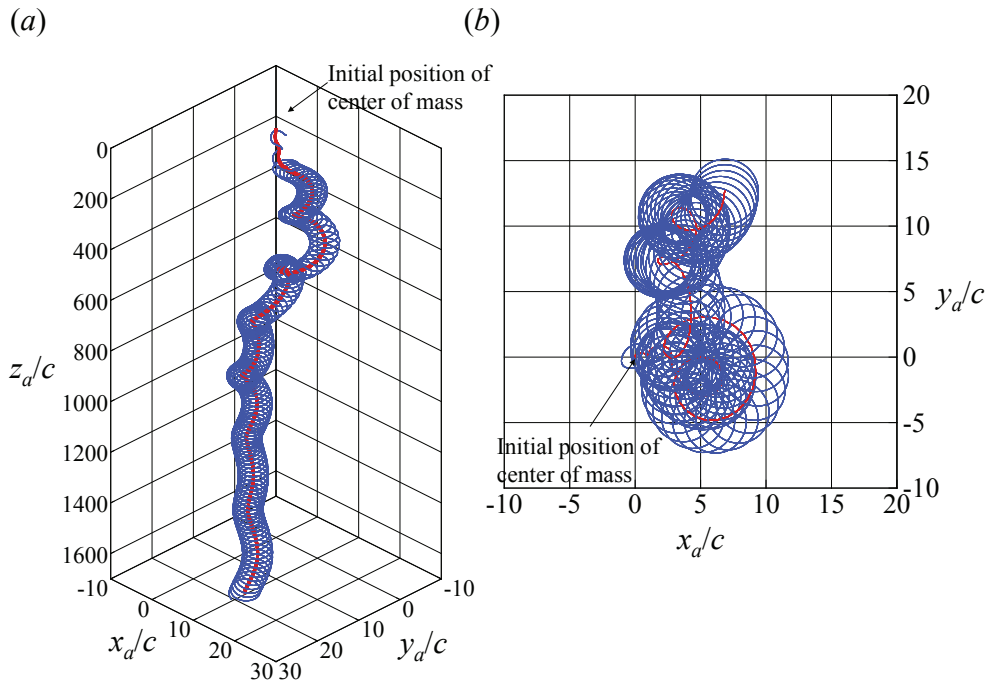

Figure 3.5. Trajectories of the center of mass (dashed red line) and wing tip (solid blue line) of the seed model in free fall: (a) overall descending and rotating trajectories in a scaled view; (b) trajectories from top view.

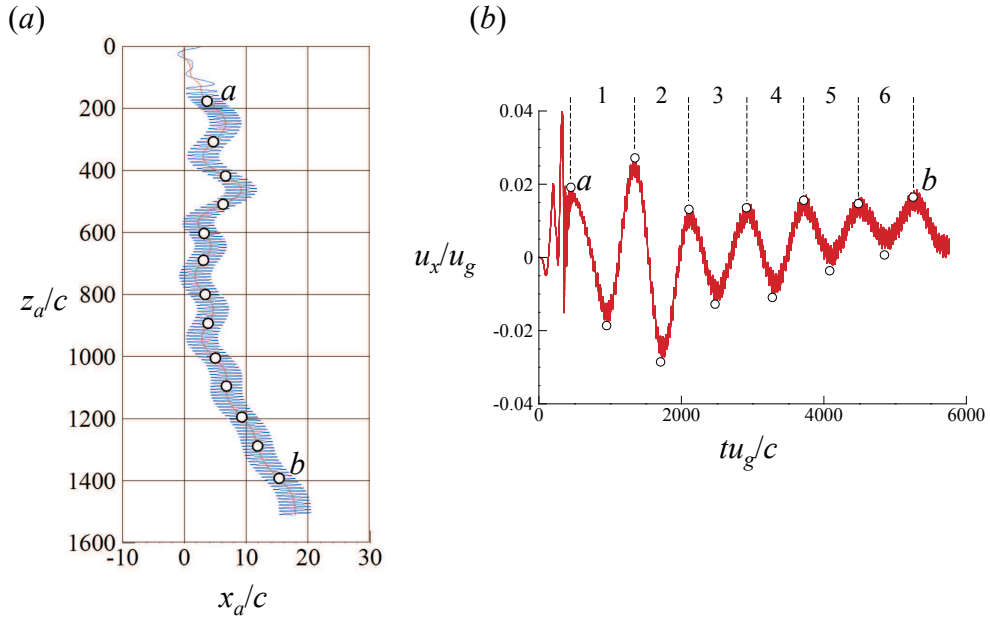

Figure 3.6. (a) Projected falling trajectories of center of mass and wing tip; (b) time trace of horizontal velocity of center of mass.

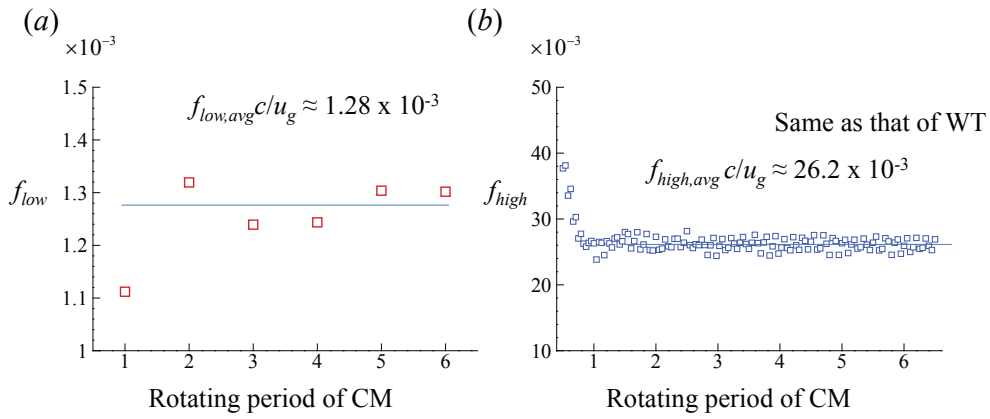

Figure 3.7. Characteristic frequencies of center of mass: (a) low frequency; (b) high frequency.

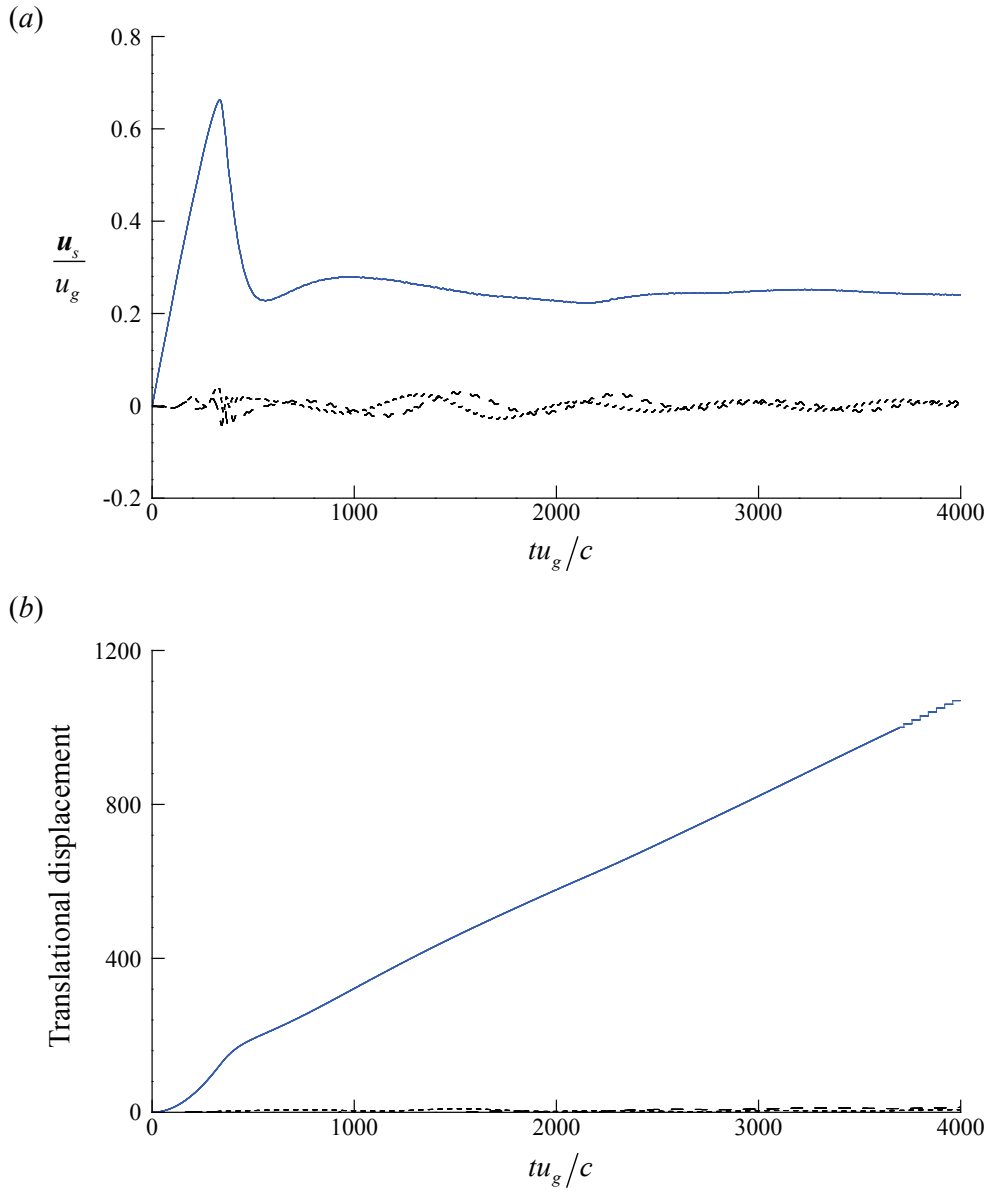

Figure 3.8. (a) Time traces of the translational velocities and displacements in inertial reference frame: (a) translational velocities; (b) translational displacements. The solid lines indicate the components of vertical direction.

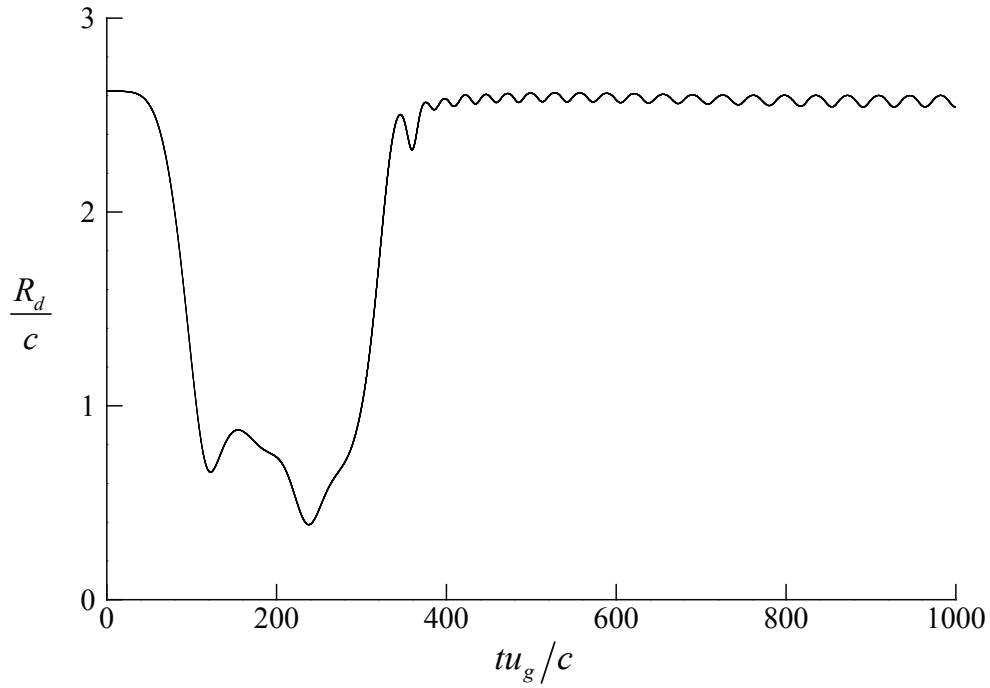

Figure 3.9. Time trace of the horizontal radius of rotation from the center of mass (at $t = 0$, the seed model is positioned in a horizontal plane and thus $R_w/c = 2.62$).

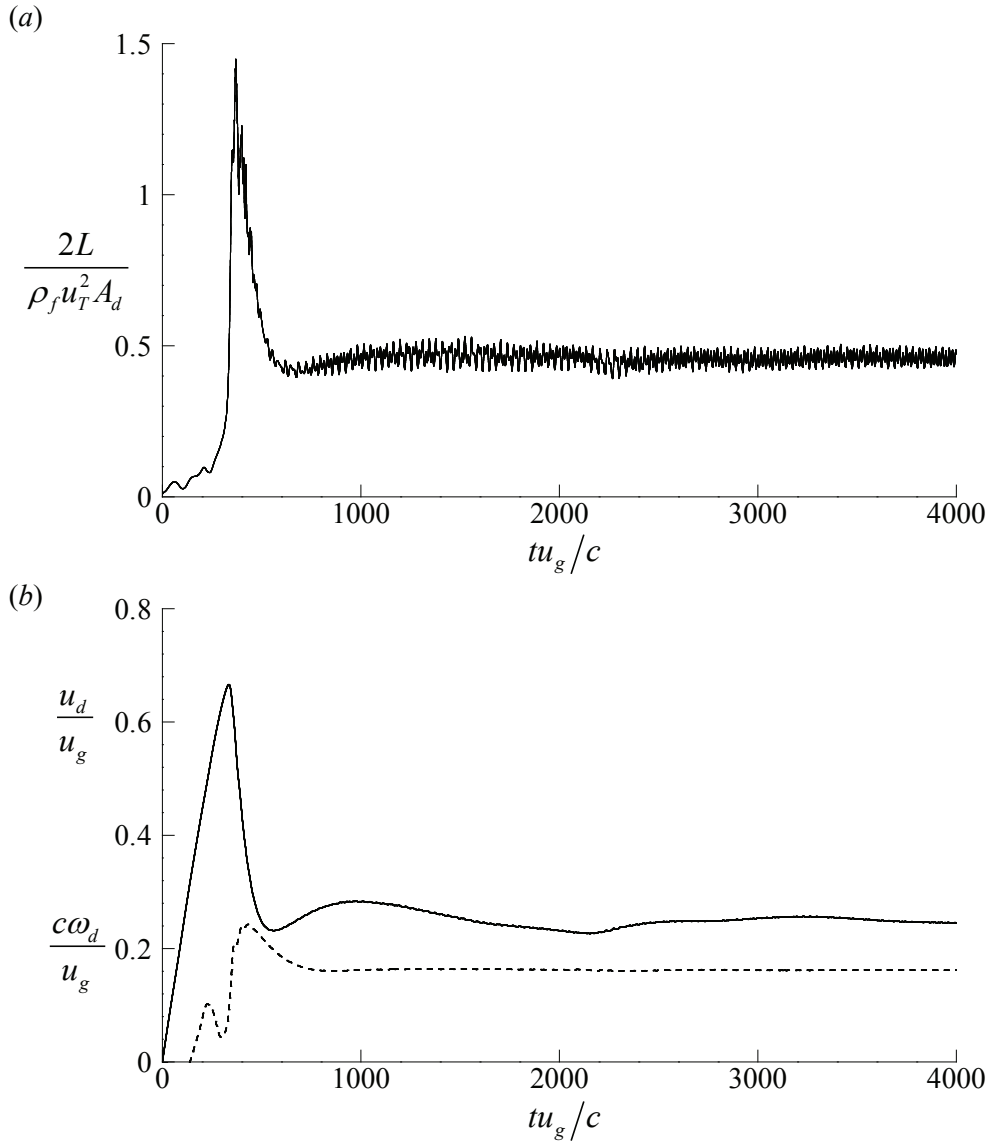

Figure 3.10. (a) Time traces of the drag coefficient; (b) time trace of the descending (solid line) and rotating (dashed line) velocities.

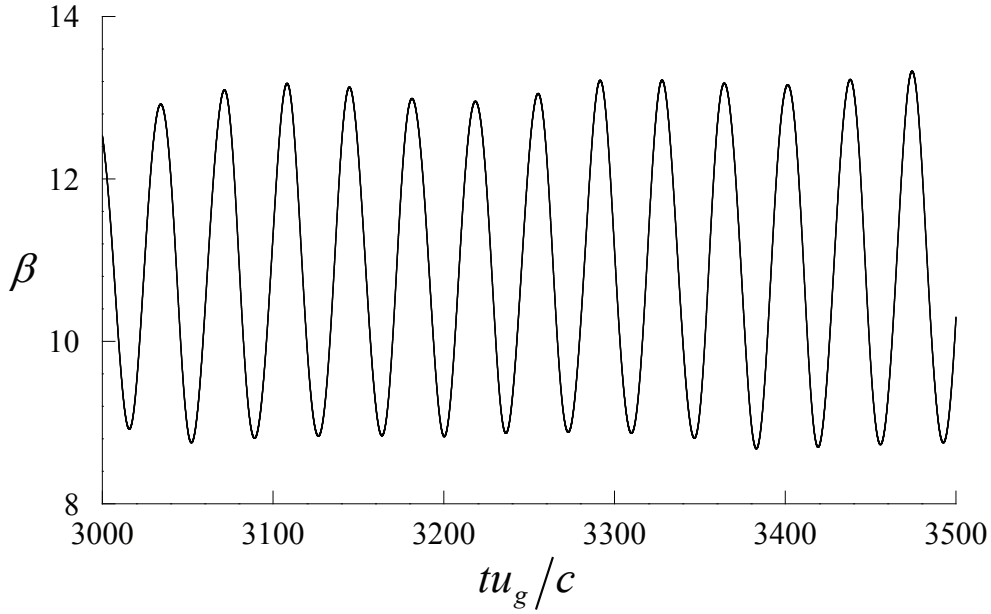

Figure 3.11. Time traces of the coning angle at steady autorotation.

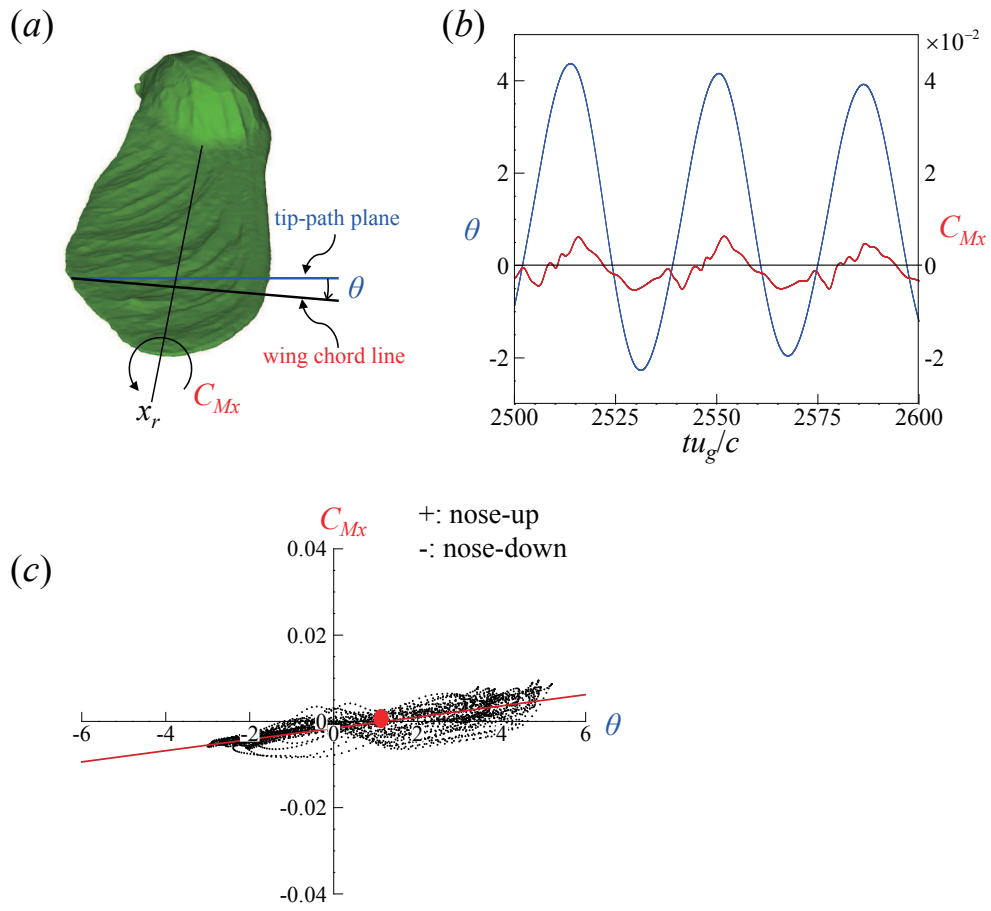

Figure 3.12. Pitching stability: (a) definition of pitching angle; (b) time traces of pitching angle (θ) and moment (C_{Mx}); (c) variation of the pitching moment coefficient with the pitching angle.

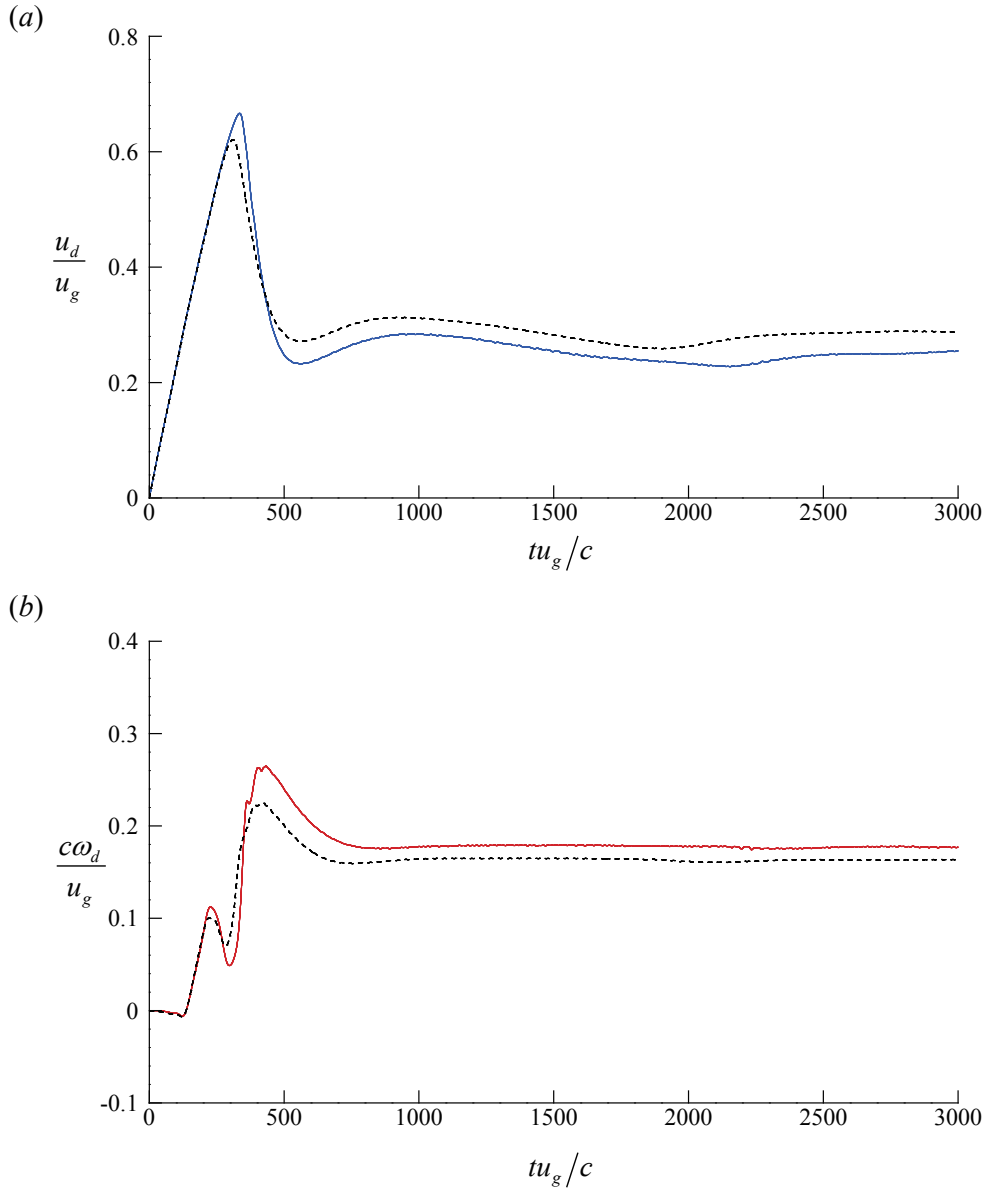

Figure 3.13. Time traces of the descending and rotating velocities for the cases with two different rotating directions: (a) descending velocity; (b) rotating velocity. The solid and dashed lines indicate the results of the seed with counter-clockwise and clockwise rotations, respectively.

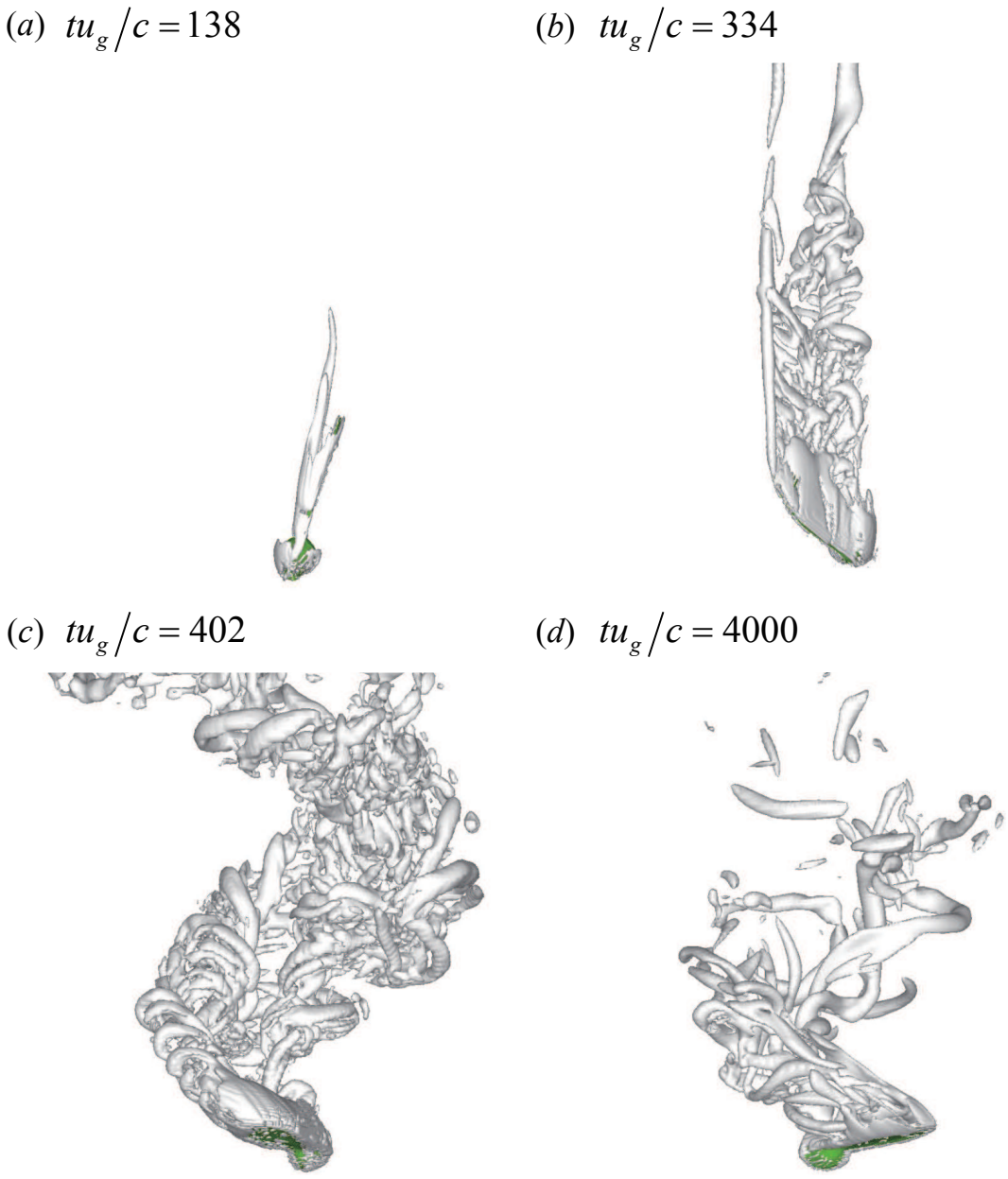

Figure 3.14. Vortical structures around the seed model at four different time instants, identified by the isosurface of $\lambda_2 = -0.1$: (a) $tu_g/c = 138$; (b) 334; (c) 402; (d) 4000. The seed model is colored in green.

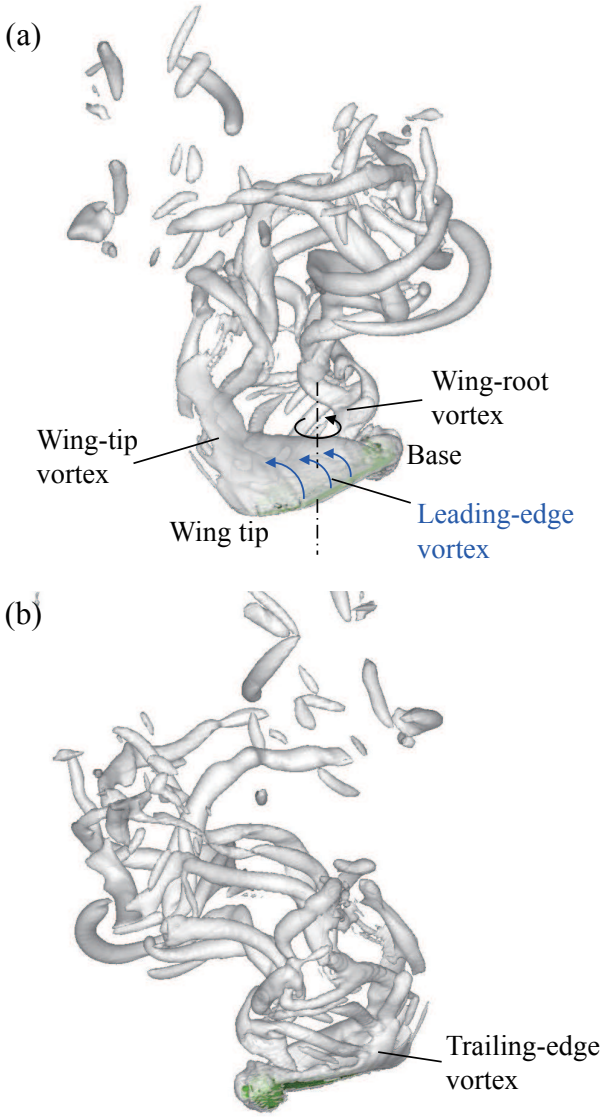

Figure 3.15. Vortical structures (wing-root, leading-edge, wing-tip, trailing-edge vortices) around the seed model at steady autorotation ($tu_g/c = 4000$), identified by the isosurface of $\lambda_2 = -0.1$: (a) windward view; (b) leeward view. The seed model is colored in green.

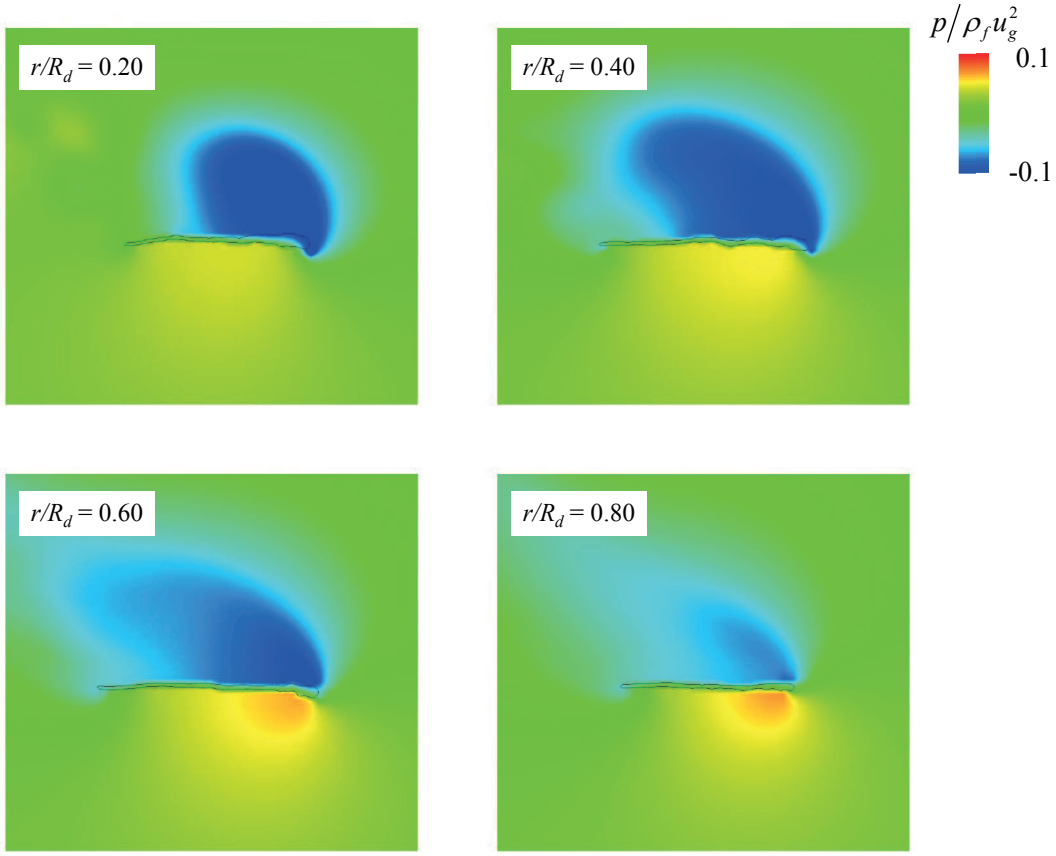

Figure 3.16. Instantaneous pressure contours around the spanwise section of rotating wing: (a) $r/R_d = 0.2$; (b) $r/R_d = 0.4$; (c) $r/R_d = 0.6$; (d) $r/R_d = 0.8$.

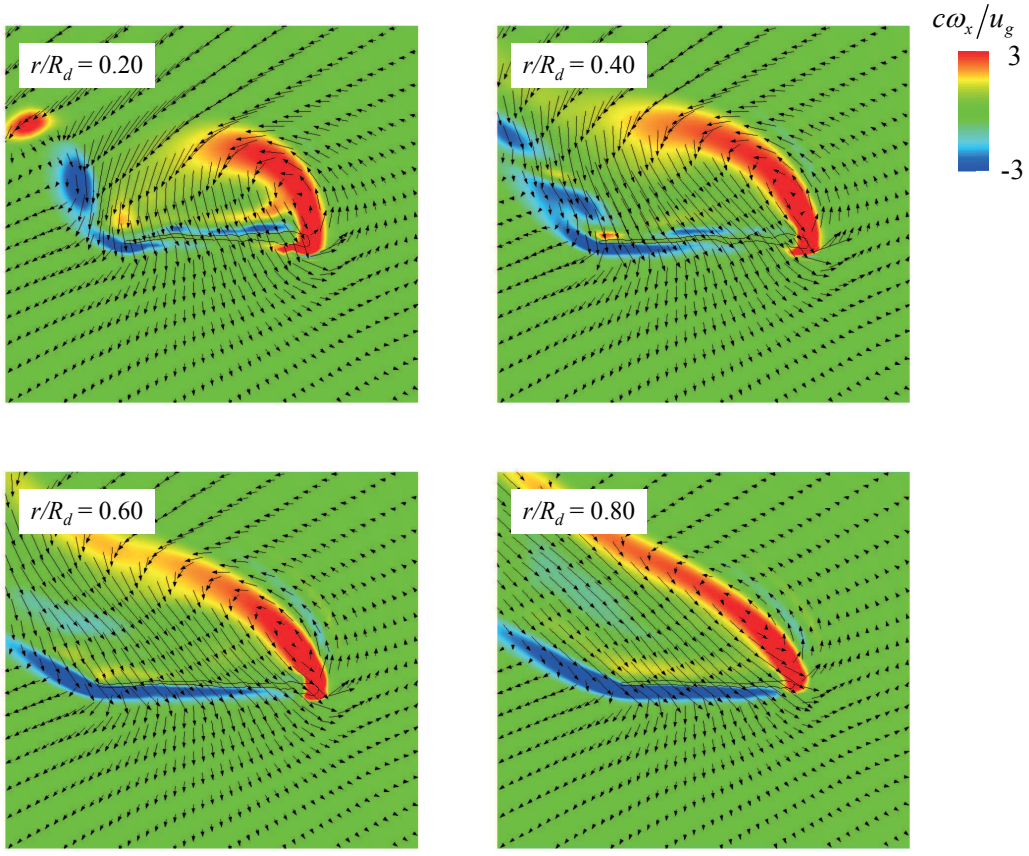

Figure 3.17. Instantaneous vorticity contours around the spanwise section of rotating wing: (a) $r/R_d = 0.2$; (b) $r/R_d = 0.4$; (c) $r/R_d = 0.6$; (d) $r/R_d = 0.8$.

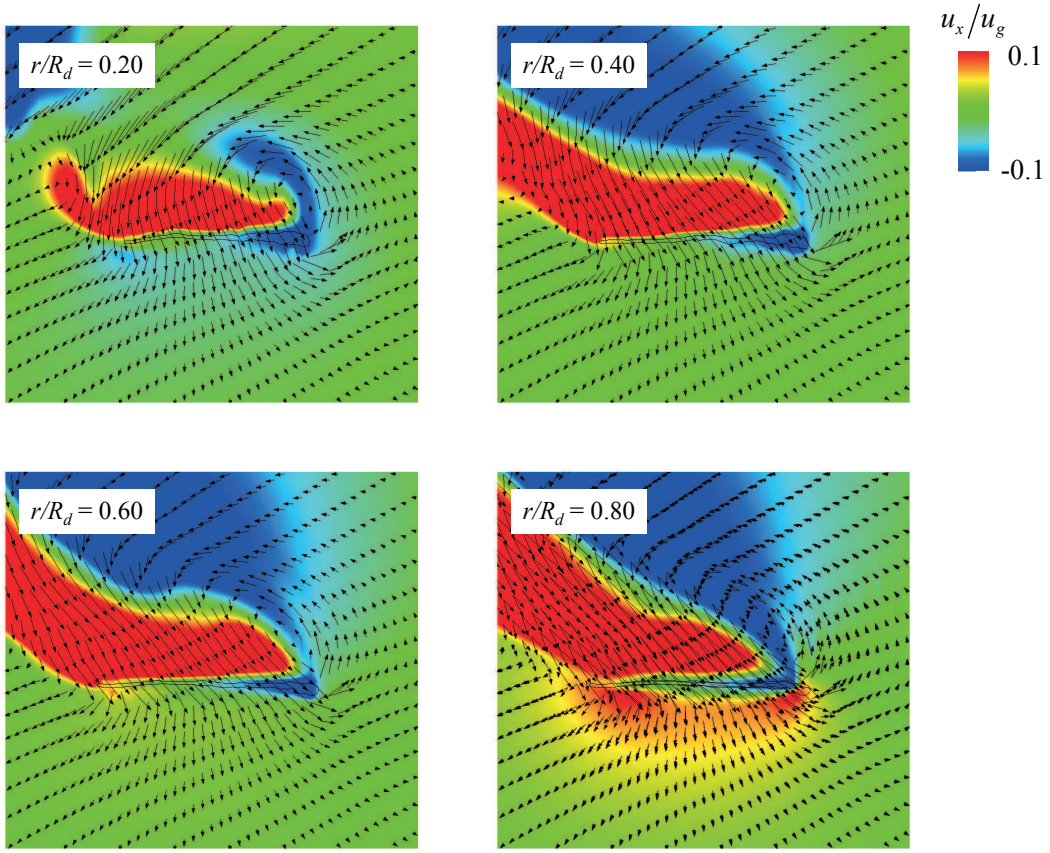

Figure 3.18. Instantaneous spanwise velocity contours around the spanwise section of rotating wing: (a) $r/R_d = 0.2$; (b) $r/R_d = 0.4$; (c) $r/R_d = 0.6$; (d) $r/R_d = 0.8$.

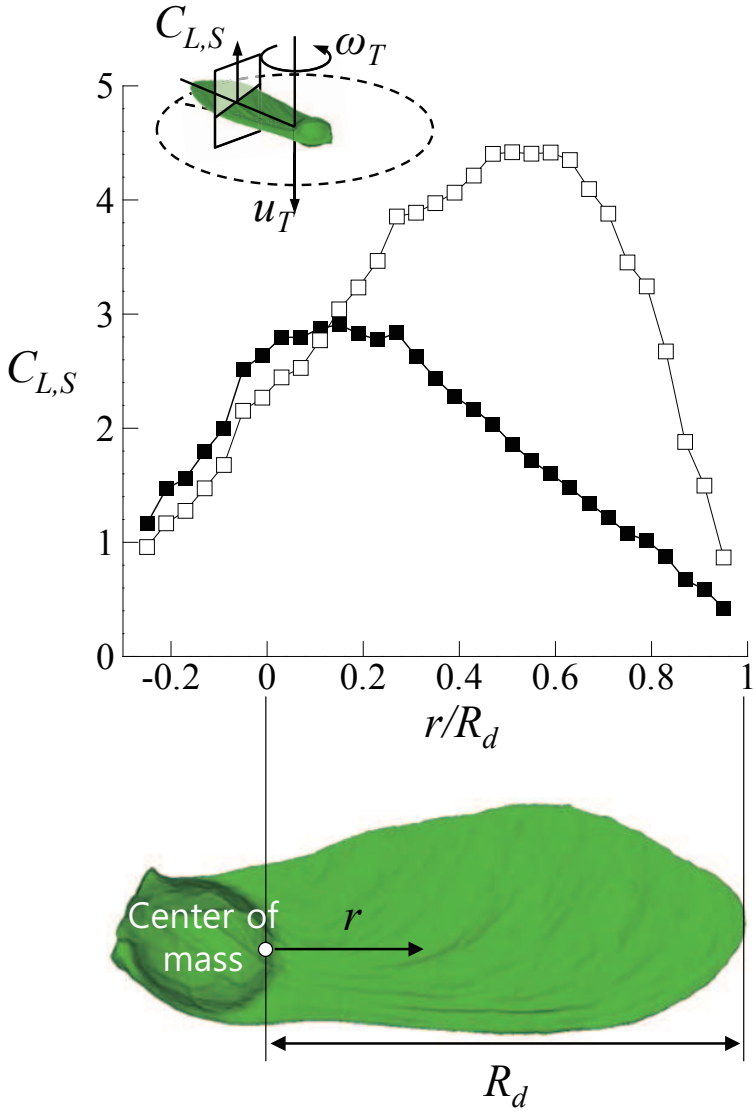

Figure 3.19. Variation of the sectional drag coefficient of the maple seed.

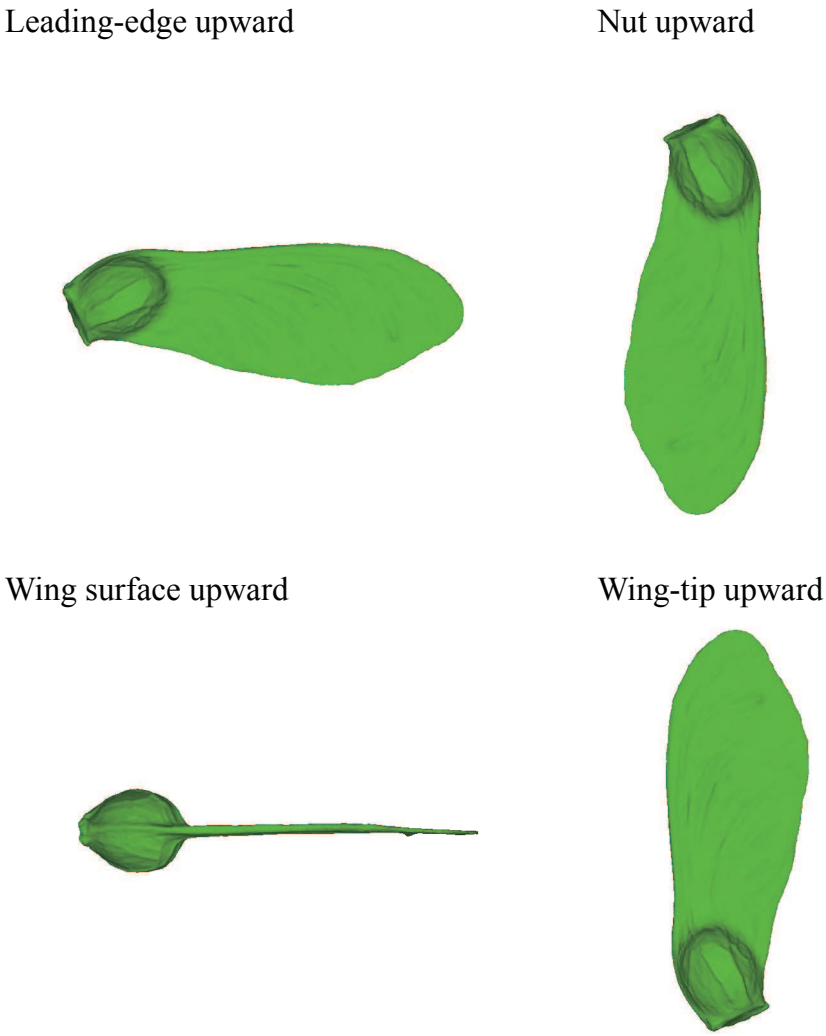

Figure 3.20. Schematic diagram of the initial posture of the seed (leading-edge upward, nut upward, wing surface upward, and wing-tip upward, respectively.)

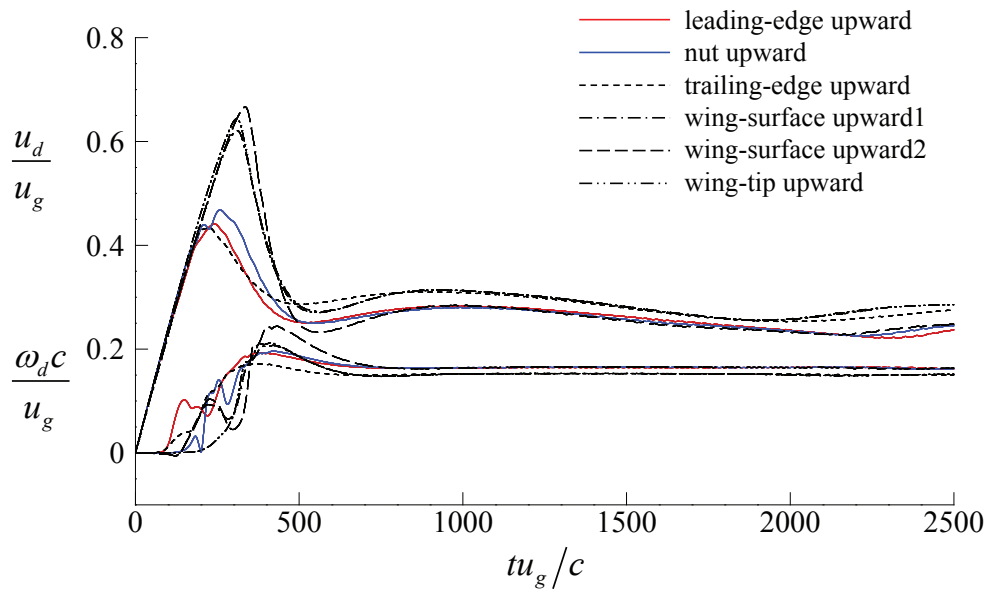

Figure 3.21. Time traces of descending and rotating velocities for autorotating seed with different initial postures.

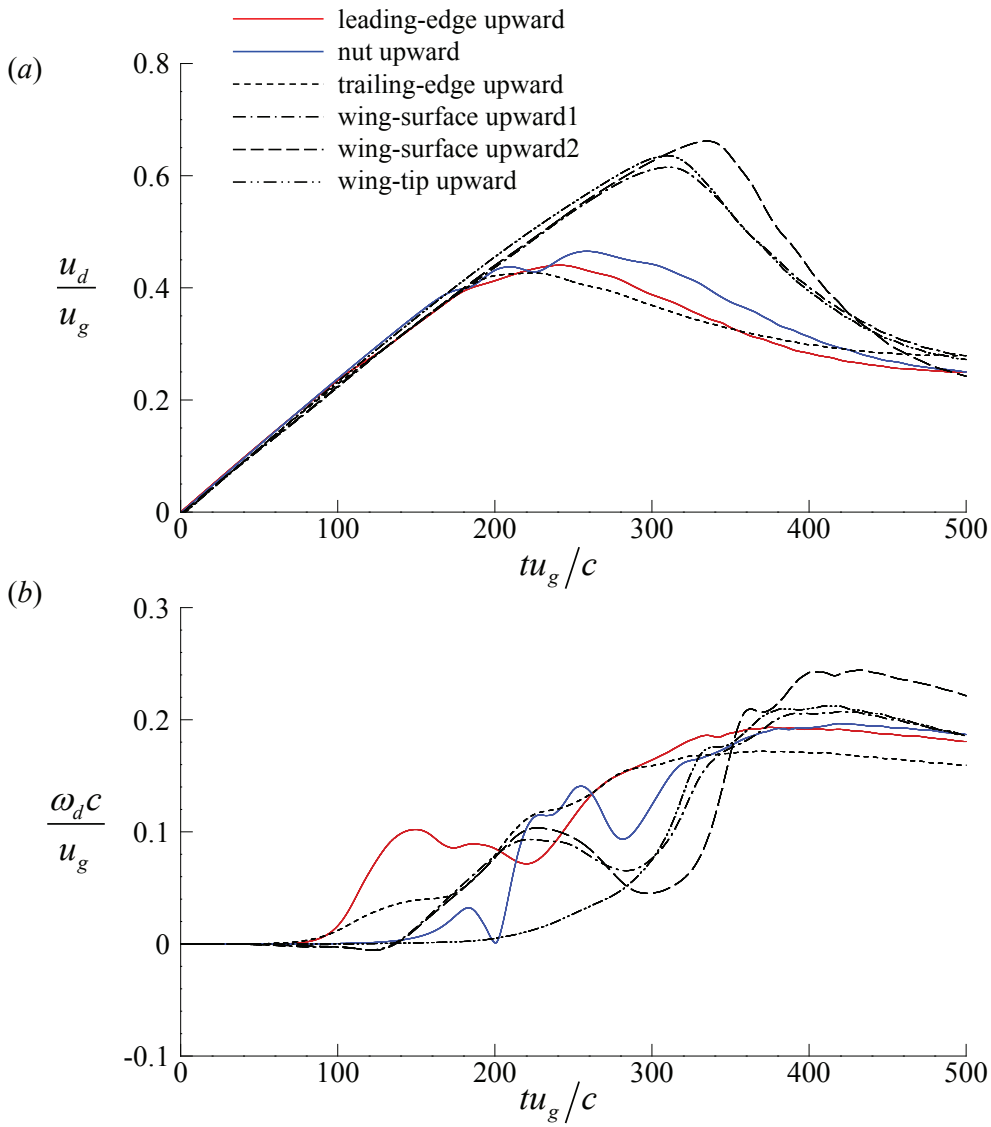

Figure 3.22. Transient region for time traces of descending and rotating velocities: (a) descending velocities; (b) rotating velocities. Solid-red line, leading-edge upward; solid-blue line, nut upward; dotted line, trailing-edge upward; dash-dot line, wing-surface upward1; dashed line, wing-surface upwrad2; dash-dotdot line, wing-tip upward.

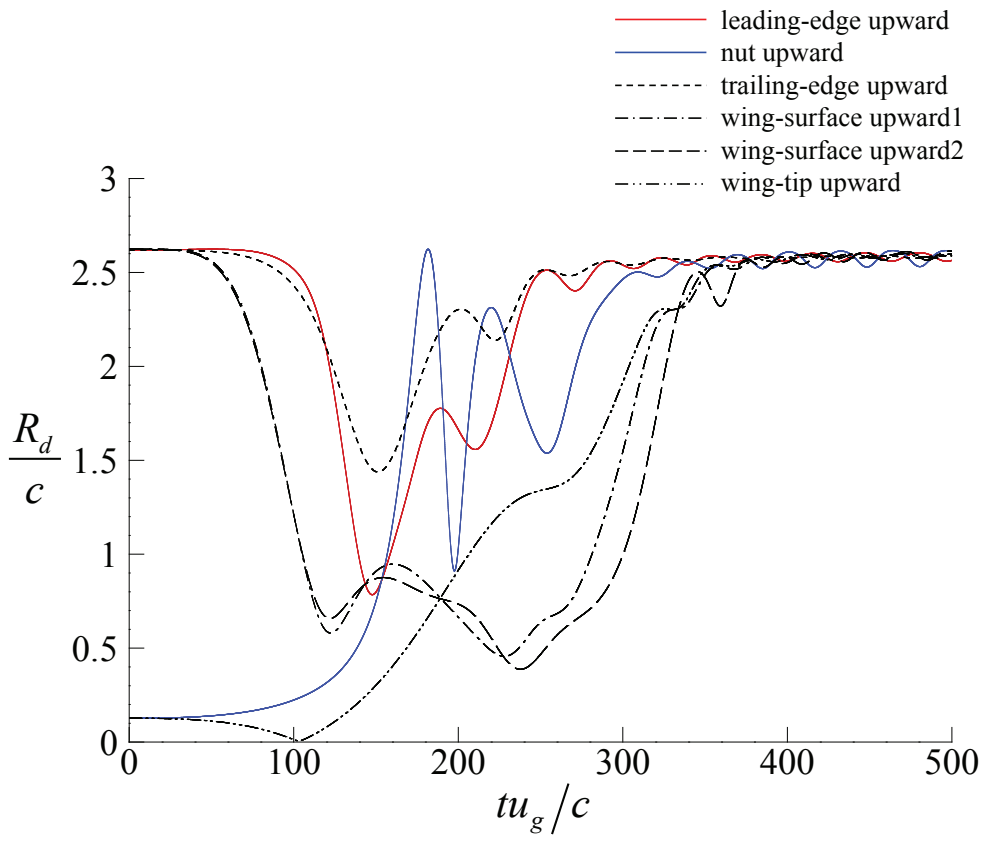

Figure 3.23. Time traces of the horizontal radius of rotation from the center of mass. Solid-red line, leading-edge upward; solid-blue line, nut upward; dotted line, trailing-edge upward; dash-dot line, wing-surface upward1; dashed line, wing-surface upwrad2; dash-dotdot line, wing-tip upward.

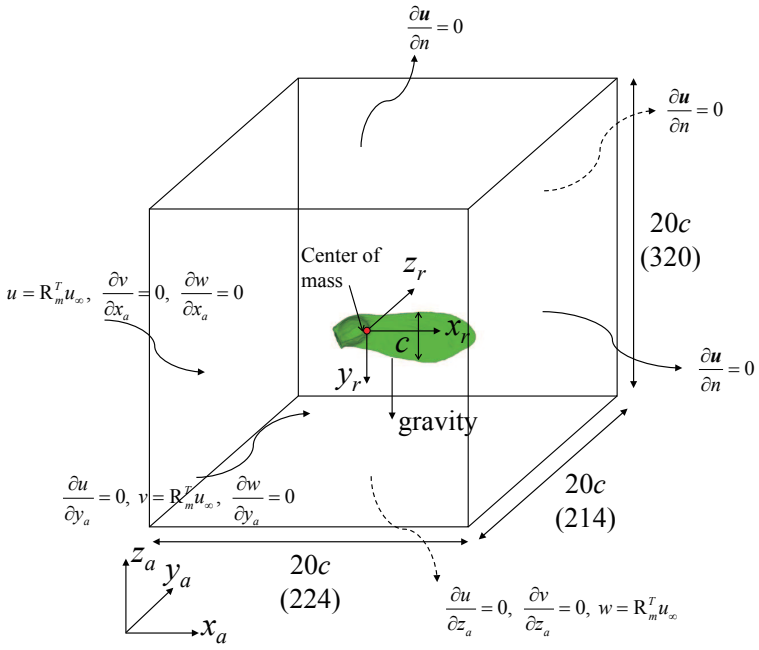

Figure 3.24. Schematic diagram of the computational domain and corresponding number of grid points with initial posture of the seed model. The boundary conditions used are shown at each boundary: Neumann and Dirichlet boundary conditions.

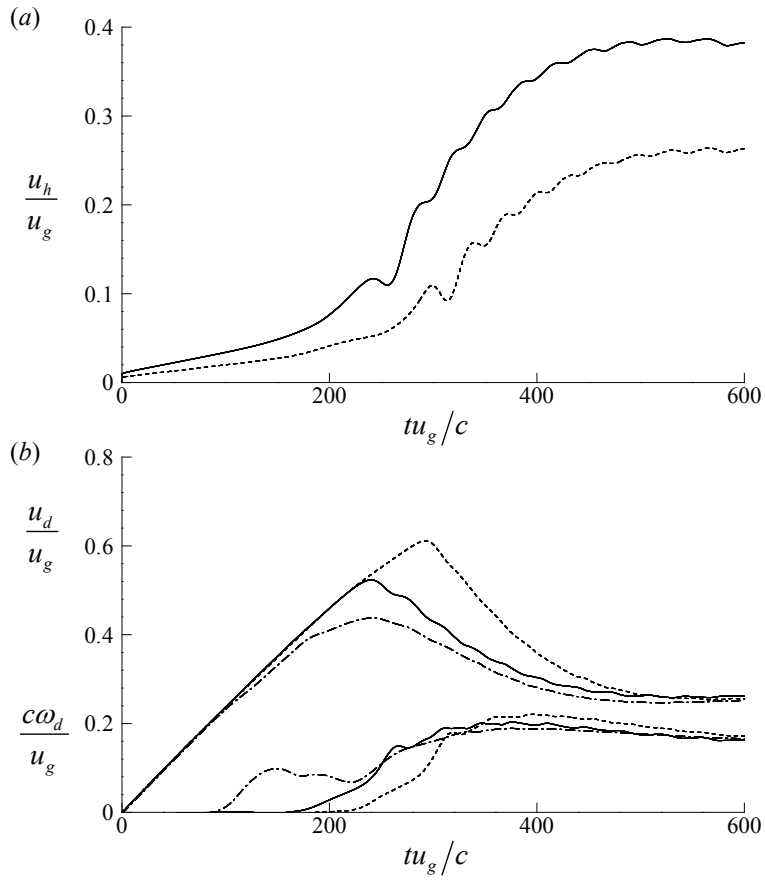

Figure 3.25. (a) Time traces of the flying velocity (same direction with wind); (b) descending and rotating velocities. The dashed and solid lines indicate the results of $u_w/u_T = 1.0$ and $u_w/u_T = 1.5$, respectively, and dash-dot line indicate that of quiescent condition.

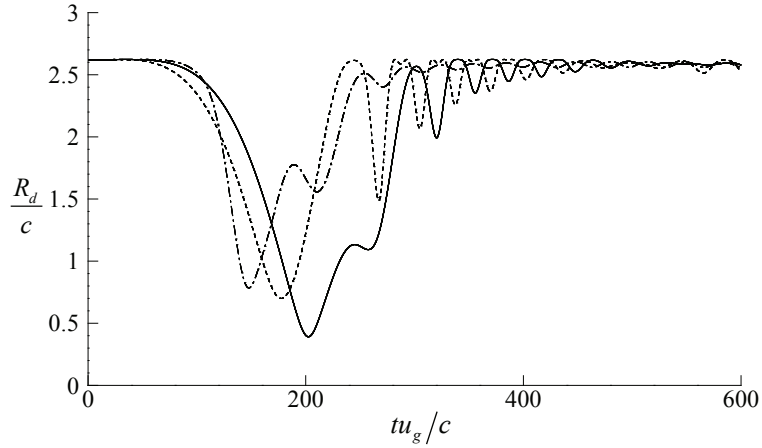

Figure 3.26. Time traces of the horizontal radius of rotation from the center of mass. The dashed and solid lines indicate the results of $u_w/u_T = 1.0$ and $u_w/u_T = 1.5$, respectively, and dash-dot line indicate that of quiescent condition.

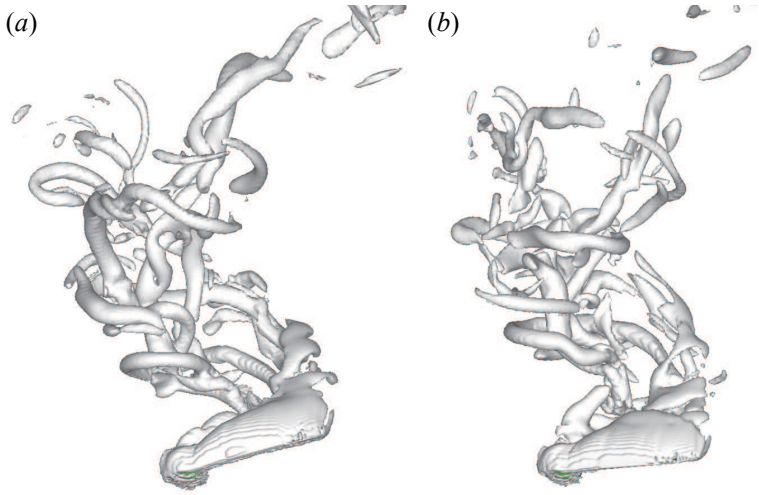

Figure 3.27. Vortical structures around the seed model: (a) $u_w/u_T = 1.0$; (b) $u_w/u_T = 1.5$.

Chapter 4

Theoretical analyses for autorotating seeds

Theoretical analyses are performed to elucidate a relation between morphological and kinematic characteristics of auturotating seeds at periodic state. For this purpose, two different approaches are adopted to obtain the drag force based on the momentum theory and potential (steady airfoil) theory. First, a theoretical model for the drag is suggested through the momentum theory for wind turbine based on the mass, linear and angular momentum, and energy conservations (Glauert, 1935; Phillips, 2002; Hunsaker & Phillips, 2013). Here, a model constant (axial induction factor) appeared during theoretical derivation is obtained from flow fields of present high-fidelity numerical simulation rather than arbitrary approximation (Azuma & Yasuda, 1989). The obtained model constant is almost same with that of direct calculation of wight of the seed indicating the accuracy of the suggested present model. Moreover, it shows that the circumferential velocity at the wake can be modelled as Rankine vortex model rather than rigid body rotation model (unrealistic special case). In addition, a scaling law for the drag of autorotating seeds is constructed through the strength of leading edge vortex from steady airfoil theory (Newmann, 1977) and the momentum induced by the vortical structure (Lee, Choi & Kim, 2015). The scaling law is also applied to sectional drag force obtained from high-fidelity numerical simulation, and it shows that the sectional drag coefficient at each wing element collapses onto a straight line indicating the suitability of the scaling law

for the drag of autorotating seeds. This scaling model provides good collapse of existing measurement data (Norberg, 1973; Azuma & Yasuda, 1989; Salcedo *et al.*, 2013; Lee, Lee & Sohn, 2014), and thus it can captures the morphological and kinematical characteristics of autorotating seeds.

4.1 Simple analysis based on the momentum theory

When a seed falls with autorotation, is has terminal descending and rotating velocities, u_T and ω_T, respectively (figure 4.1(a)). Using the Galilean transformation with the terminal descending velocity u_T, the seed rotates at the terminal rotating velocity ω_T with zero descending velocity (figure 4.1(b)). Norberg (1973) employed the axial momentum theory and derived a relation of $mg/A_d \propto u_T^2$, where A_d is the disk area, and mg/A_d is the disk loading (m is the mass of the seed, and g is the gravitational acceleration). Therefore, other things being equal, the terminal descending velocity of a seed is proportional to the square root of its disk loading. The same relation holds for hovering animals of any size, with the modification that it is the air flowing through the wing disk that is accelerated to a final velocity proportional to the square root of the disk loading (Norberg, 1973). Subsequently, an optimal model of $mg/A_d = \rho_f {u_T}^2/2$ was suggested by Azuma & Yasuda (1989) by requiring the axial velocity in far wake u_w to be zero. It follows that for a given set of geometric parameters, terminal velocity of a seed cannot be less than that obtained from optimal or lower limit expressions (figure 4.2). However, all the experimental data are scattered above the minimum rate of descent, and Azuma & Yasuda (1989) described that the difference between the theoretical and actual results probably comes from the limits of the simple momentum theory. Although their theoretical contributions are quite meaningful to understand the nature

of autorotating seeds, these analyses did not consider the angular momentum conservation, and the latter study neglected the mass conservation in obtaining the optimal condition. It has been shown that neglecting the effects of wake rotation is not conservative approach to drag estimation (Hunsaker & Phillips, 2013). Therefore, it is required to employ both the angular and linear momentum conservation, and suggest an improved theoretical model for the drag based on the flow characteristics of autorotating seeds at periodic state.

The procedure of obtaining the drag force acting on an autorotating seed is very similar to those of wind turbines, called wind turbine theory (Glauert, 1935). It starts using the mass, linear and angular momentum and energy conservations with an inviscid flow approximation before and after the seed, and is briefly introduced below. The detailed procedure to derive the drag can be found from the previous study introducing a momentum theory with slipstream (Hunsaker & Phillips, 2013). The momentum theory is based on the hypothesis of a streamtube, which encloses the disk, and this streamtube is assumed to extend infinitely far upstream (inflow) from the disk to a plane infinitely far downstream (wake) (Hunsaker & Phillips, 2013). All the fluid that enters the streamtube on the far upstream side must pass through the disk and exit the streamtube on the far downstream side. Assuming an inviscid flow before (inflow to 1) and after (2 to far wake) the disk (i.e. a rotating seed) (figure 4.1(b)), the Bernoulli equation is applied to these regions:

$$\frac{p_\infty}{\rho_f} + \frac{1}{2}u_T^2 = \frac{p_1}{\rho_f} + \frac{1}{2}\left(u_{z1}^2 + u_{r1}^2 + u_{\theta 1}^2\right), \tag{4.1}$$

$$\frac{p_2}{\rho_f} + \frac{1}{2}\left(u_{z2}^2 + u_{r2}^2 + u_{\theta 2}^2\right) = \frac{p_w}{\rho_f} + \frac{1}{2}\left(u_{zw}^2 + u_{rw}^2 + u_{\theta w}^2\right), \tag{4.2}$$

where, u_{zi}, u_{ri}, and $u_{\theta i}$ are the axial, radial, and circumferential velocities,

respectivley, and p_i are the pressures. Here, the subscript i indicate the axial location (inflow, 1, 2, or far wake).

From the angular momentum conservation (inflow to 1), $u_{\theta 1} = 0$, from continuity (1 to 2), $u_{z1} = u_{z2}$, and from no lateral force on the disk, $u_{r1} = u_{r2}$. Here it is assumed that the axial velocity component u_{zi} varies only along the axial direction. At the far wake, the flow properties are independent of axial position and circumferential position, and the continuity equation requires that

$$\frac{\partial \left(r_w u_{rw} \right)}{\partial r_w} = 0, \tag{4.3}$$

and it gives $u_{rw} = 0$ subject to the outer boundary condition which specifies that there is no radial component of velocity at the edge of the ultimate slipstream (Hunsaker & Phillips, 2013).

The three components of the reduced momentum equation in the slipstream are

$$u_{rw} \frac{\partial u_{rw}}{\partial r_w} - \frac{u_{\theta w}^2}{r_w} = -\frac{1}{\rho_f} \frac{dp_w}{dr_w}, \tag{4.4}$$

$$u_{rw} \frac{\partial u_{\theta w}}{\partial r_w} - \frac{u_{rw} u_{\theta w}}{r_w} = 0, \tag{4.5}$$

$$u_{rw} \frac{\partial u_{zw}}{\partial r_w} = 0. \tag{4.6}$$

As a result, a relation for radial pressure gradient at the far wake can be obtained from above continuity and momentum equations incorporating solid body rotation assumption in the wake (Hunsaker & Phillips, 2013):

$$\frac{dp_w}{dr_w} = \rho_f \frac{u_{\theta w}^2}{r_w} = \rho_f \omega_w^2 r_w. \tag{4.7}$$

From equation (4.7), at far wake, $p_w = p_\infty - \rho_f \omega_w^2 (R_w^2 - r_w^2)/2$ because

the pressure must be equal to the freestream pressure at the outer edge of the slipstream at the far wake and the assumption of solid body rotation ($u_{\theta w} = r_w \omega_w$) (Hunsaker & Phillips, 2013). The mass and angular momentum conservations for the control volume (2 to far wake) provide $r_d^2 u_{z2} = r_w^2 u_{zw}$ and $r_d u_{\theta 2} = r_w u_{\theta w} = r_w^2 \omega_w$, respectively. Then, from equations (4.1) and (4.2), the pressure difference across the disk is obtained as

$$\frac{p_2 - p_1}{\rho_f} = -\frac{1}{2}\left(u_T^2 - u_{zw}^2\right) - \frac{\omega_w^2}{2}\left[R_d^2 - \left(2 - \frac{u_{z2}}{u_{zw}} r_d^2\right)\right]. \tag{4.8}$$

Therefore, the drag force (D) on the disk is obtained by integrating equation (4.8) over the disk area:

$$\begin{aligned} D &= -\int_0^{R_d} (p_2 - p_1)\, 2\pi r_d dr_d \\ &= \frac{1}{2}\pi \rho_f R_d^2 \left(u_T^2 - u_{zw}^2 + \frac{R_d^2}{2}\omega_w^2 \frac{u_{z2}^2}{u_{zw}^2}\right). \end{aligned} \tag{4.9}$$

By equating the drag force in equation (4.9) to that obtained from the axial momentum conservation for the control volume from inflow to far wake, a relation between u_{z2}, u_T, and u_{zw} is obtained as $u_{z2} = (u_T + u_{zw})/2$. Note that this relation is the same with that developed from axial momentum theory. Also from the angular momentum and energy conservations for the control volume (inflow to far wake) is obtained as (Phillips, 2002; Hunsaker & Phillips, 2013).

$$\omega_w = -\left[\left(u_T^2 - u_{zw}^2\right)/\omega_T R_d^2\right](u_{zw}/u_{z2}), \tag{4.10}$$

With this relation, equation (4.9) becomes

$$D = 2\pi\rho_f R_d^2 a(1-a)u_T^2\left[2a\left(1-a\right)\frac{u_T^2}{R_d^2\omega_T^2}+1\right], \tag{4.11}$$

where a $(= 1 - u_{z2}/u_T)$ is a model constant, called the axial induction factor (Glauert, 1935). Then the non-dimensional drag coefficient becomes

$$C_D = \frac{2L}{\rho_f u_T^2 \pi R_d^2} = 4a\left(1-a\right)\left[2a\left(1-a\right)\left(\frac{u_T}{R_d\omega_T}\right)^2+1\right]. \tag{4.12}$$

The obtained model yields a solution for the drag coefficient that is a function of tip-speed ratio ($\lambda = R_d\omega_T/u_T$) while the classical (axial) momentum theory predicts that the drag is independent of tip-speed ratio (Hunsaker & Phillips, 2013). Note that this relation approaches the model for drag from axial momentum theory $C_D = 4a(1-a)$ as the tip-speed ratio approaches infinity $R_d\omega_T/u_T \to \infty$.

As seen from equation (4.12), the drag force coefficient can be determined by the terminal descending and rotating velocities, only if the model constant, axial induction factor a, is known. Note also that the disk radius R_d is not exactly same as that of the wing span R_w because descending seeds have a coning angle of about $13^\circ \backsim 17^\circ$ for the maple seed (*Acer palmatum*) in Azuma & Yasuda (1989). In the present study, the axial induction factor can be obtained from the flow field rather than arbitrary approximations such as $a = 0.5$ from maximum drag force (Azuma & Yasuda, 1989). Figure 4.3 shows the schematic diagram for disk regions along the axial directions to measure the axial induction factor and the instantaneous contour of axial induction factor. By increasing the axial position $z_a/R_d = 0$ to $z_a/R_d = 0.2$, axial induction factor is obtained with the relation of $a = 1 - u_{z2}/u_T$, where u_{z2} is the velocity component normal to

the rotating disk at each axial position. Figure 4.4 shows the period-averaged contours of axial induction factor during five revolutions of the maple seed at steady autorotation. In addition, by averaging these axial induction factor along circumferential direction, radial distributions of axial induction factor at each axial position are obtained (figure 4.5(a)). As shown, the axial induction factor increases by increasing the axial position at the core region while it decreases by increasing the axial position at the outer region. Finally, mean values of axial induction factor over whole disk area can be obtained and are shown in figure 4.5(b). As shown, the mean axial induction factor increases almost linearly along axial positions after the disk. Because the maple seed rotate having coning angle β as shown in figure 4.3(a), it is required to define the axial induction factor as averaged value for the volume consisting of disk area from center of mass to wing tip of the seed (from $z_a/R_d = 0$ to $z_a/R_d = 0.175$). The obtained value from the present high fidelity simulation is $a = 0.126$, and is much less than that of optimal case ($a = 0.5$) obtained by Azuma & Yasuda (1989). As mentioned earlier, Azuma & Yasuda (1989) obtained a =0.5 for maximum drag generation assuming the axial velocity at far wake was zero. However, this assumption violates the mass conservation and thus $a = 0.5$ is not realizable. The obtained model constant is almost same with that of direct calculation of wight of the seed indicating the accuracy of the suggested theoretical model for the drag ($a = 0.121$ from direct calculation with the weight of maple seed, mg $= 1.13 \times 10^{-4}$ $kg{\cdot}m/s^2$).

Because the drag force is equal to the seed weight at the periodic state, the disk loading mg/A_d of the seed has the following relate from equation 4.12:

$$\frac{mg}{\rho_f A_d u_T^2} = 2a\,(1-a)\left[2a\,(1-a)\left(\frac{u_T}{R_d\omega_T}\right)^2 + 1\right], \tag{4.13}$$

where $A_d(= \pi R_d^2)$ is the disk area. This model provides a simple relation between the disk loading and terminal velocities of the autorotating seed.

Figure 4.6 shows the axial induction factor versus disk loading for various autorotating seeds. Here, the axial induction factor is calculated by inserting the weight of the seed directly to equation 4.13. As shown in figure 4.6(b), the axial induction factor is almost same with the results from conventional momentum theory, $mg/\rho_f u_T^2 A_d = 2a(1-a)$, (Azuma & Yasuda, 1989). This means that the effect of rotating motion is small as compared to that of axial motion.

On the other hand, the present model is based on the assumption of the rigid body rotation of the fluid at the wake region that is an unrealistic special case. This implies that the circulation needs to increase as $\Gamma \sim r^2$ and that the loading consequently has to increase as $L \sim r^3$, which is not physical (Sørensen, 2016). Here, the circumferential velocity distributions are investigated to confirm the previous assumption of the rigid body rotation at the wake and suggest more realistic model for circumferential velocity after the disk (figure 4.7). In this figure, the contours of period-averaged circumferential velocities during five revolutions of the maple seed are presented by increasing the axial positions at the wake region. Apparently, the circumferential velocity increases along the radial direction as the rigid body rotation, but it decreases after a certain radial position. Figure 4.8 shows the radial distribution of circumferential velocities which are averaged along circumferential direction. From the numerical results, it can be estimated that the circumferential velocity distribution as a Rankine vortex model (rigid body rotation within a core and decay of angular velocity outside) in the wake than whole rigid body rotation assumption (figure 4.8). Then, by repeating the previous procedures of momentum theory, the drag coefficient can be expressed as

$$C_D = 4a\,(1-a)\left[\frac{8a\,(1-a)}{(2-R_r^2/R_d^2)^2\lambda^2}\left(\frac{1}{4}-\ln\frac{R_r}{R_d}\right)+1\right]. \tag{4.14}$$

This improved model for the drag can be used to model the blade of wind turbine (thrust in this case) as well as characterize the morphological and kinematic properties of autorotating seeds. Figure 4.9 shows the weight of the seeds versus scaling parameter. Available data from winged seeds is applied to the present scaling laws, showing collapse onto scaling laws than previous one (Azuma & Yasuda, 1989).

4.2 Scaling law for the drag of autorotating seed

Here, the scaling analysis is performed as similar to that of previous study for the drag of hovering insects based on the potential theory (Lee, Choi & Kim, 2015). In general, two kinds of forces act on the wing, one due to added mass and the other due to circulation (Lee *et al.*, 2013). The force due to added mass is generated as the velocity of wing changes as in flight of many insect wing, but in the present study, the descending and rotating velocities are constant (terminal velocities) at periodic state. Therefore, the force generated by added mass is almost negligible. The force due to circulation, vortical force, is the time derivative of the vortical impulse (M_V). The vortical impulse is determined by the vorticity distribution in the flow field, and intense vorticity is distributed around the plate edge where the separation of vortical structures occurs (Lee *et al.*, 2013). Therefore, the magnitude of the vortex impulse M_V can be approximated using a vortex loop model: $M_V \sim \rho_f \Gamma R_d c$, where Γ is the strength of the vortex loop (Dickinson, 1996; Lee, Choi & Kim, 2015). The shear flow separated at the leading edge of autorotating seeds spirals into the leading edge vortex, and thus the strength of the leading edge vortex is related

to that of the shear flow generated on the wing, which is modelled as vortex sheets in the classical steady aerofoil theory.

The strength of the leading edge vortex via circulation around a three-dimensional wing (Newmann, 1977), Γ, is scaled as

$$\Gamma \sim \frac{Uc}{1 + 2c/R_d}\text{sin}\alpha, \tag{4.15}$$

where U is the free-stream velocity, α is the angle of attack, c is the mean chord length, R_d is the disk radius (figure 4.10(a)). Lee, Choi & Kim (2015) measured the vorticity of flows around a flat plate translating linearly at high angles of attack within a water tank and showed that this model provides a reasonable approximation for the strength of the leading edge vortex on wings operated in hovering conditions by varying the wing velocity, stroke distance, angle of attack, wing span and chord length.

As mentioned before, the momentum induced by the vortical structure, M_V, is approximated as $M_V \sim \rho_f \Gamma R_d c$, and the reaction force exerted on the wing due to the time derivative of vortical impulse is scaled as $F \sim M_V/T \sim \rho_f \Gamma R_d c/T$, where T is the rotating period. Note that the circulatory force is almost perfectly normal to the surface of the wing at angles of attack above 15° (Dickinson, 1996), and this is also satisfied in the present study of autorotating seed because the angle of attack α at the wing tip reaches about 30° (figure 4.11). For autorotating seeds, the linear velocity of the wing U and rotating period T can be scaled as $U \sim \sqrt{R_d^2\omega_T^2 + u_T^2}$ and $T = 2\pi/\omega_T$, respectively, and $\text{sin}\alpha = u_T/U$. Therefore, the circulation around the leading edge vortex can be scaled as $\Gamma \sim u_T c/(1 + 2c/R_d)$ using the scaling relation, equation (4.15). By combining these relations, the scaling approximations of the drag force is obtained as

$$D \sim \frac{1}{2\pi}\frac{\rho_f u_T \omega_T R_d c^2}{1+2c/R_d}. \tag{4.16}$$

At the periodic state, the drag force D balances the weight mg of the seed, and thus the scaling approximation for the weight of autorotating seed is same with equation (4.16). The weight of the seed normalized by the dynamic pressure force, $0.5\rho_f U^2 R_d c$, with the characteristic wing tip velocity U and the projected wing area $R_d c$, is scaled as

$$\frac{2mg}{\rho_f U^2 R_d c} \sim \frac{c\omega_T}{\pi u_T(\lambda^2+1)}\frac{1}{1+2c/R_d}, \tag{4.17}$$

where λ is the tip speed ratio defined as $\lambda = R_d\omega_T/u_T$. This indicate that the suggested model captures the morphological and kinematical characteristics of autorotating seeds from simple potential theory.

On the other hand, unlike the hovering insects wing, the angle of attack α is varying along the wing span (figure 4.11) resulting in the variation of local speed ratio $\lambda_r = r_d\omega_T/u_T$. Therefore, it is required to verify the scaling law whether it is also valid for the sectional drag force coefficient of autorotating seeds. Figure 4.10(b) shows the schematic diagram for the sectional drag on the rotating wing. For a spanwise section, the sectional drag force $\Delta D(r)$ is scaled as based on equation (4.16):

$$\Delta D(r) \sim \frac{1}{2\pi}\frac{\rho_f u_T \omega_T c(r)^2}{1+2c(r)/R_d}\Delta r, \tag{4.18}$$

where $c(r)$ is the chord length at each element and Δr is the section length at each element. Therefore the normalized sectional drag force can be scaled as

$$\frac{2\Delta D(r)}{\rho_f U(r)^2 c(r)\Delta r} \sim \frac{c(r)\omega_T}{\pi u_T[(r/R_d)^2\lambda^2+1]}\frac{1}{1+2c(r)/R_d}, \tag{4.19}$$

As mentioned before, the present scaling law is based on the strength of the leading edge vortex via circulation around a three-dimensional wing. In the previous chapter (section 3.5), the sectional drag coefficients are calculated for the spanwise regions of base to wing tip, and it shows that the portion of the drag force acting on the wing (center of mass to wing tip) is about 9 times greater than that on the nut (base to center of mass). It means that the rotating wing play a prominent role in generating the drag force, and thus it is appropriate that present scaling law is applied to the regions only including the rotating wing of the seed except the nut (figure 4.11). Note that the autorotating seeds descend having a pitching angle θ which is varying along the wing span due to the aerodynamic balance as well as structural twisting and undulating characteristics. However, since the experimental observations did not report the pitching angle distribution θ along the wing span, the pitching angle is not considered in the calculation of the angle of attack α at each spanwise section, $\alpha_r = \alpha$ - θ is the actual angle of attack, figure 4.12(a)). For example ,in the present simulation, the time-averaged value of pitching angle at $r/R_d = 0.75$ is about $\theta_{mean} = -1.23^\circ$ (figure 4.12(b)), and thus this value is very small as compared with the angle of attack α (figure 4.11).

Figure 4.13 shows the sectional drag coefficient obtained from the present simulation according to the dimensionless scaling law in equation (4.19). As shown, all of the sectional drag coefficients collapse onto a straight line, indicating the appropriateness of the present scaling law for the drag estimation of autorotating seeds even though the angle of attack is varying along the span (equation 4.17). Based on this result, the present model, equation (4.17), is compared with the measurement data of various autorotating seeds from previous studies (Norberg, 1973; Azuma & Yasuda, 1989; Salcedo *et al.*, 2013; Lee, Lee & Sohn, 2014). The morphological and kinematic parameters of various

autorotating seeds are shown in table 4.1 which are from previous studies (Norberg, 1973; Azuma & Yasuda, 1989; Salcedo *et al.*, 2013; Lee, Lee & Sohn, 2014) including those of present study. Figure 4.14 shows the relation between weight and scaling parameters. Previous measurement data and present result from high-fidelity numerical simulation are plotted according to the scaling law, and the scaling law favourably agrees well with previous experimental data. As a result, this scaling law will be helpful to elucidate an essential aerodynamics of autorotating seeds easily, and provides a clear fluid dynamic explanation of how different evolutionary selections for wing kinematics and morphology among autorotating seeds can arrive at the same functionality, autorotation with similar wing loads, as similar to the hovering insect wing (Lee, Choi & Kim, 2015). Also it will be a simple yet powerful guideline for designing auturotation-based micro air vehicles such as SAMARAI monocoptor developed by Lockheed Martin and Common Smart Submunition developed by Textron (Crimi, 1988).

4.3 Summary

In this chapter, theoretical analyses were conducted to obtain scaling laws describing the relation among the seed weight and geometry, and descending and rotating velocities. The first uses the conservation of mass, linear and angular momentum, and energy. In this approach, a model constant to be determined, called the axial induction factor, is obtained from the result of present simulation. The second approach employs a classical steady wing theory in which the vortical strength is scaled with the circulation around a wing and the lift force is modeled by the time derivative of vortical impulse. Available data from winged seeds are applied to the present scaling laws, showing excellent collapses onto the scaling laws. The suggested scaling model can offer a simple and pow-

	m $(\times 10^{-6} kg)$	c $(\times 10^{-3} m)$	R_w $(\times 10^{-3} m)$	R_d $(\times 10^{-3} m)$	u_T m/s	ω_T rad/s	β ^{o}
(a)	58.58	8.4	36.2	28.49	0.82	102.3	23.7
(b)	38	6.6	25.2	20.96	1.04	115.3	27.6
(c)	13	3.8	14.8	11.95	1.09	189.1	15.0
(d)	23	5	21.9	17.93	0.98	154.2	20.8
(e)	229	3.8	25.5	26.64	1.58	158.9	15.6
(f)	139	10.8	52.4	36.9	1.34	87.2	16.5
(g)	23	6.1	23	17.6	1.02	101.1	12.9
(h)	98	24.3	90.1	67.3	1.14	75.2	17.2
(i)	632	22.9	92.7	71.7	1.45	44.8	20.0
(j)	42.5	6.68	22.1	19.4	1.26	133.6	19.4
(k)	130	12.22	37	35	0.9	81.7	20.0
(l)	7.5	4.09	11	10	0.64	125.7	22.0
(m)	11.5	4.27	11.19	10.98	1.02	172.3	11.3

Table 4.1. Morphological and kinematical parameters of autorotating seed: (a), *Acer diabolicum blume* (Azuma & Yasuda, 1989); (b) *Acer palmatum Thunb. Var. Matsumurae Makino* (Azuma & Yasuda, 1989); (c), *Acer palmatum Thunb.* (Azuma & Yasuda, 1989); (d), *Pinus Thunbergii Parlatore* (Azuma & Yasuda, 1989); (e), *Buckleya Joan Makino* (Azuma & Yasuda, 1989); (f), *Tilia Miqueliana Maxim.* (Azuma & Yasuda, 1989); (g), *Carpinus Tschonoskii Maxim.* (Azuma & Yasuda, 1989); (h), *Firmiana platanifolia Schott et Endl.* (Azuma & Yasuda, 1989); (i), *Swietenia macrophylla* (Salcedo *et al.*, 2013); (j), *Acer palmatum* (Lee, Lee & Sohn, 2014); (k), *Acer platanoides* (Norberg, 1973); (l), *Picea abies* (Norberg, 1973); (m), *Acer palmatum* (present)

erful guideline for biologists and engineers who seek the evolutionary direction of morphologies and kinematics of autorotating seeds and design autorotation-based MAVs, respectively.

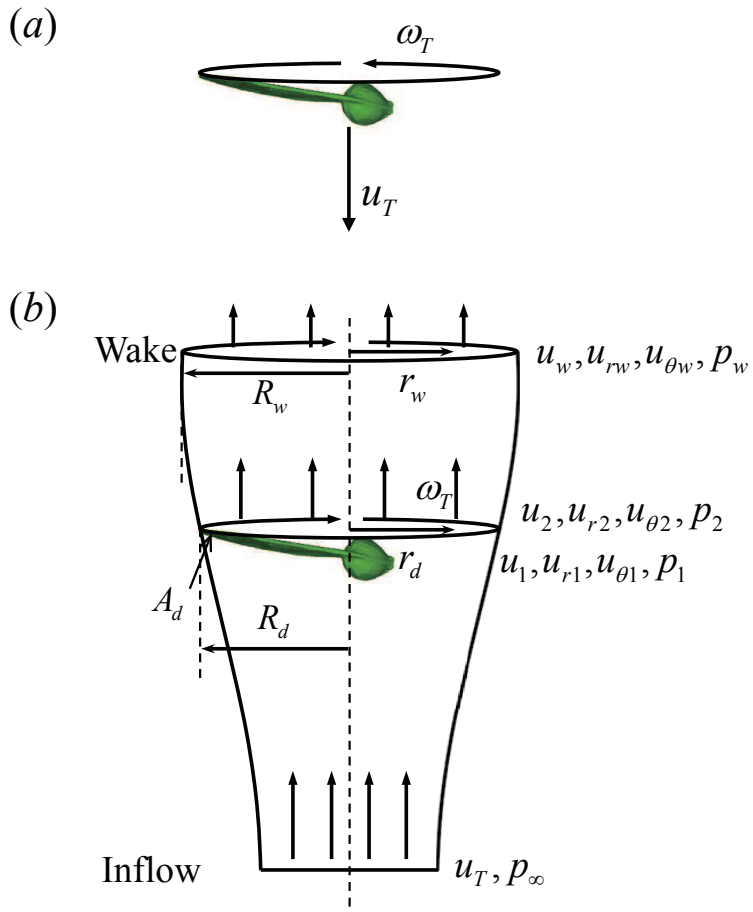

Figure 4.1. (a) Schematic diagram of an autorotating seed at periodic state; (b) control volume for the linear momentum conservations. In (a), u_T is the terminal descending velocity. In (b), (u_{zi}, u_{ri}, $u_{\theta i}$) are the axial, radial and circumferential velocities, respectively, and p_i are the pressures. Here, the subscript i indicate the axial location (inflow, 1, 2, or far wake). A_d is the disk area spanned by rotation of a seed, and R_d and r_d are the disk radius and the radial direction, respectively.

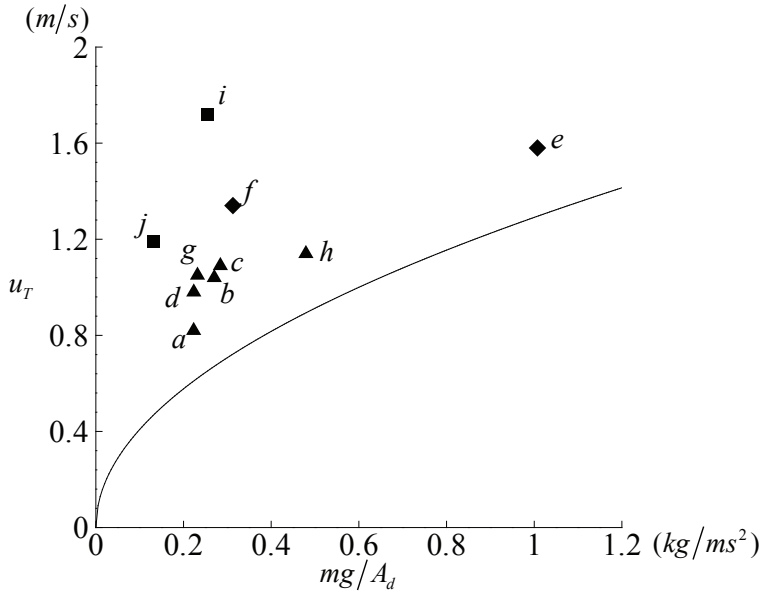

Figure 4.2. Descending velocity (u_T) and disk loading (mg/A_d) (Azuma & Yasuda, 1989): *a*, *Acer diabolicum blume*; *b Acer palmatum Thunb. Var. Matsumurae Makino*; *c*, *Acer palmatum Thunb.*; *d*, *Pinus Thunbergii Parlatore*; *e*, *Buckleya Joan Makino*; *f*, *Tilia Miqueliana Maxim.*; *g*, *Carpinus Tschonoskii Maxim.*; *h*, *Firmiana platanifolia Schott et Endl.*; *i*, *Fraxinus japonica Blume*; *j*, *Liriodendron tulipifera L.*. ▲, autorotating single-winged seeds without tumbling; ♦, autorotating multiple-winged seeds without tumbling ; ■, autorotating single-winged seeds with tumbling.

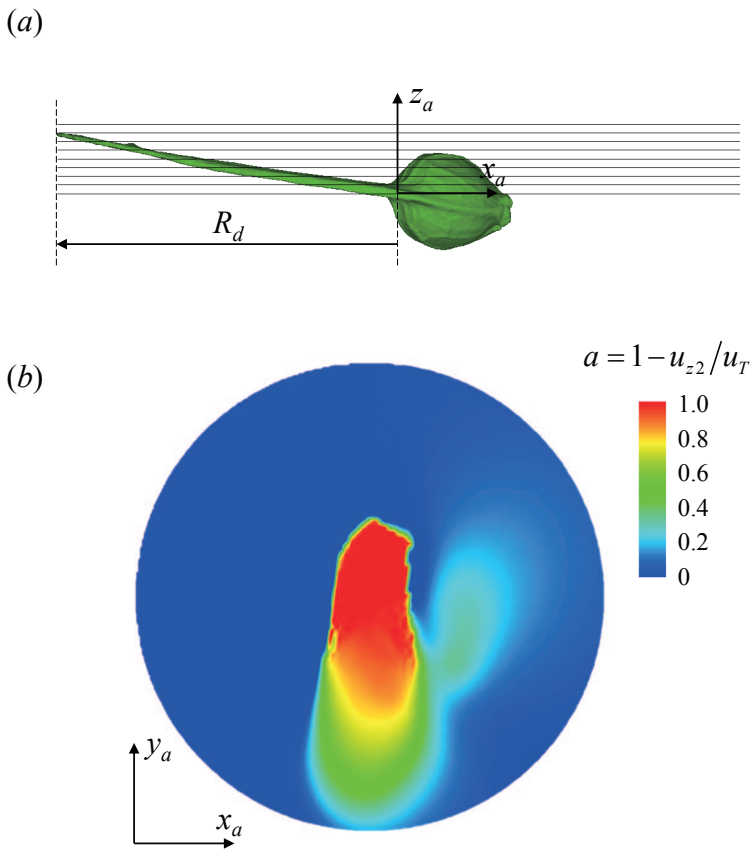

Figure 4.3. (a) Schematic diagram for disk regions along the axial directions to measure the axial induction factor; (b) instantaneous contour of the axial induction factor at $z_a/R_d = 0$.

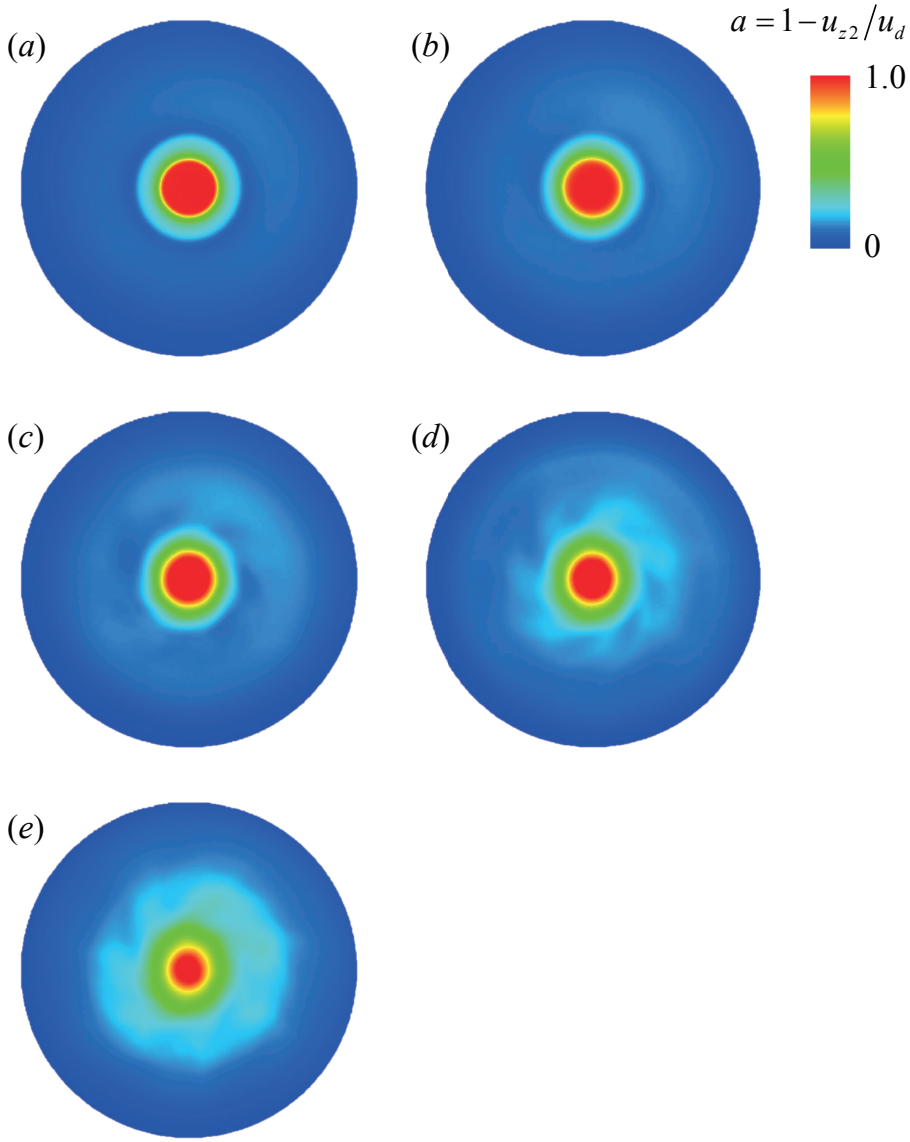

Figure 4.4. Period-averaged contours of axial induction factor during five revolutions of the maple seed at steady autorotation: (*a*) $z_a/R_d = 0$; (*b*) $z_a/R_d = 0.5$; (*c*) $z_a/R_d = 1.0$; (*d*) $z_a/R_d = 1.5$; (*e*) $z_a/R_d = 2.0$.

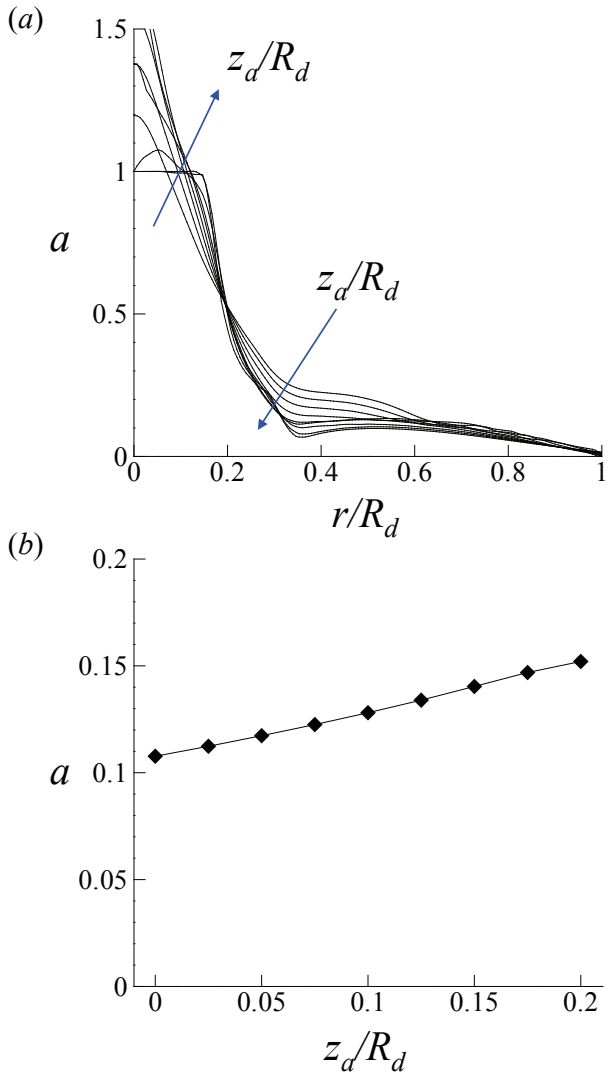

Figure 4.5. (a) Radial distributions of period-averaged axial induction factor at each axial position; (b) distribution of volume-averaged axial induction factor.

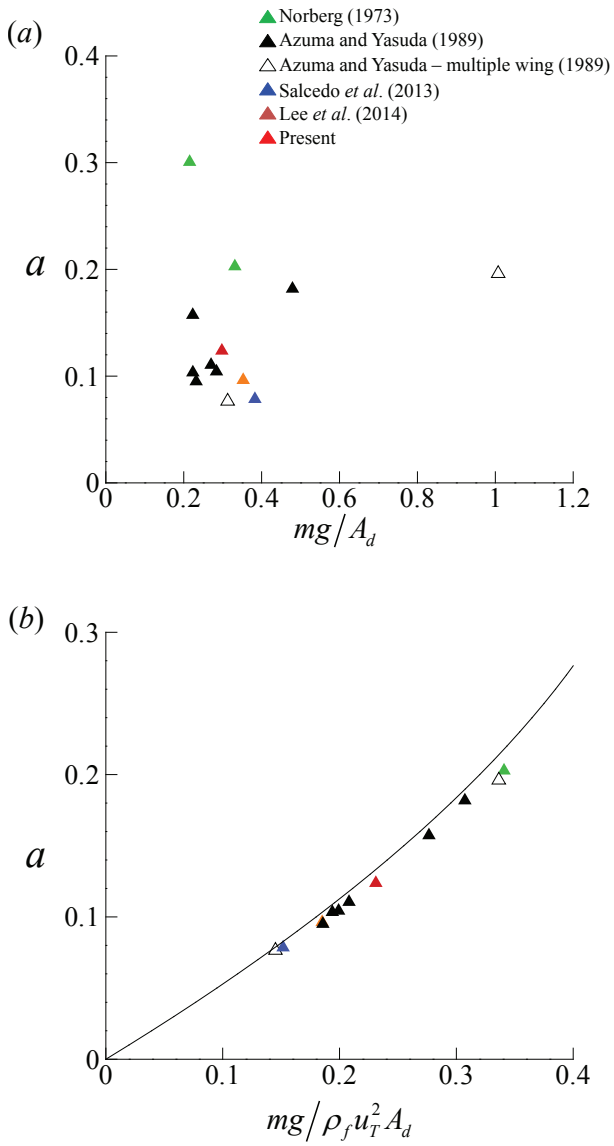

Figure 4.6. Axial induction factor versus disk loading: (a) dimensional disk loading; (b) non-dimensionalized disk loading. In (b), the solid line denotes the result of conventional momentum theory, $mg/\rho_f u_T^2 A_d = 2a(1-a)$.

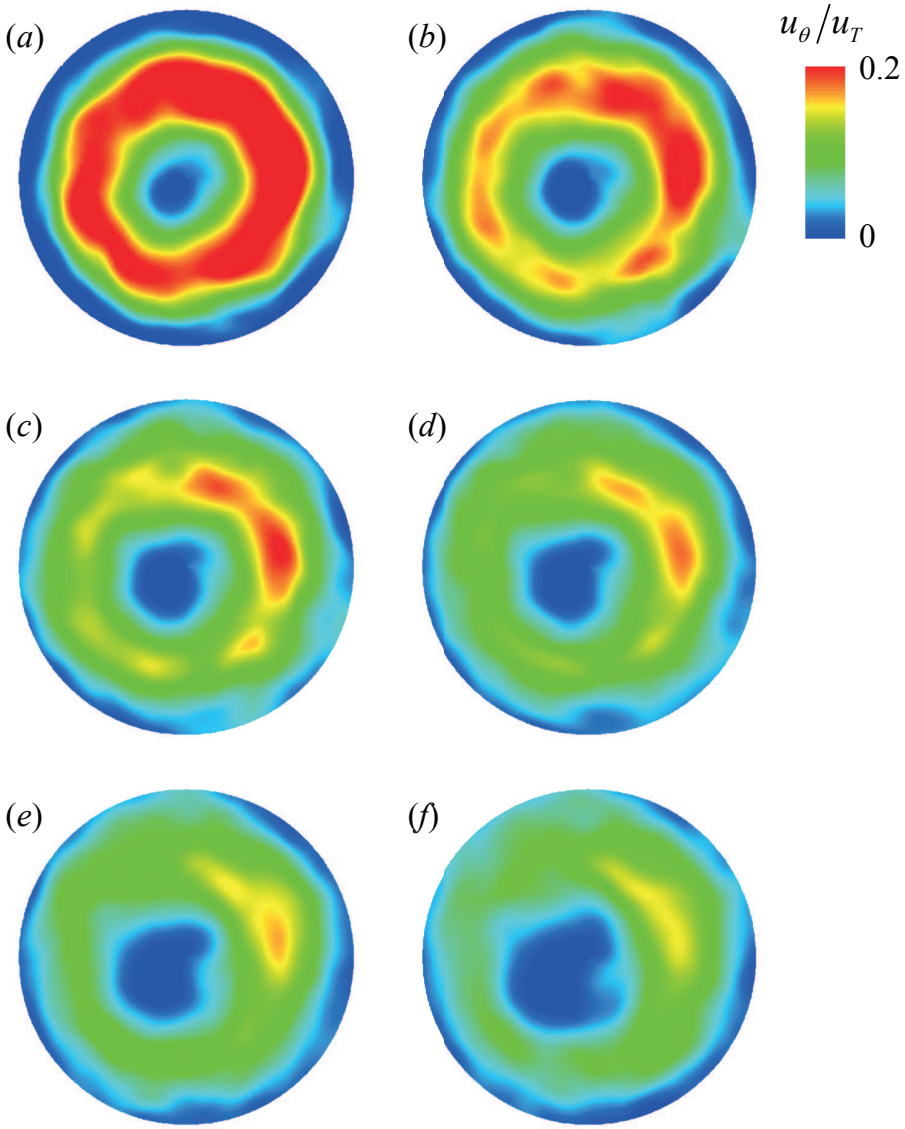

Figure 4.7. Contours of period-averaged circumferential velocities during five revolutions of the maple seed by increasing the axial positions at the wake region: (a) $z_a/R_d = 1.2$; (b) $z_a/R_d = 1.6$; (c) $z_a/R_d = 2.0$; (d) $z_a/R_d = 2.4$; (e) $z_a/R_d = 2.8$; (f) $z_a/R_d = 3.2$.

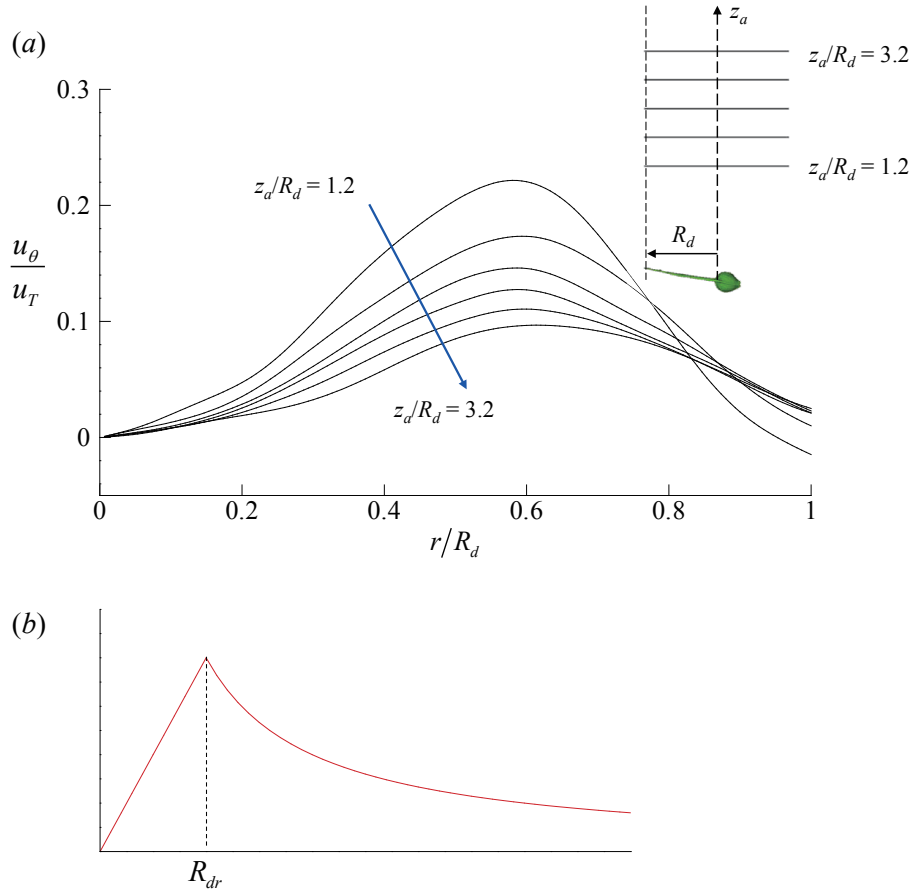

Figure 4.8. (a) Radial distribution of circumferential velocities which are averaged along circumferential direction; (b) Rankine-vortex model.

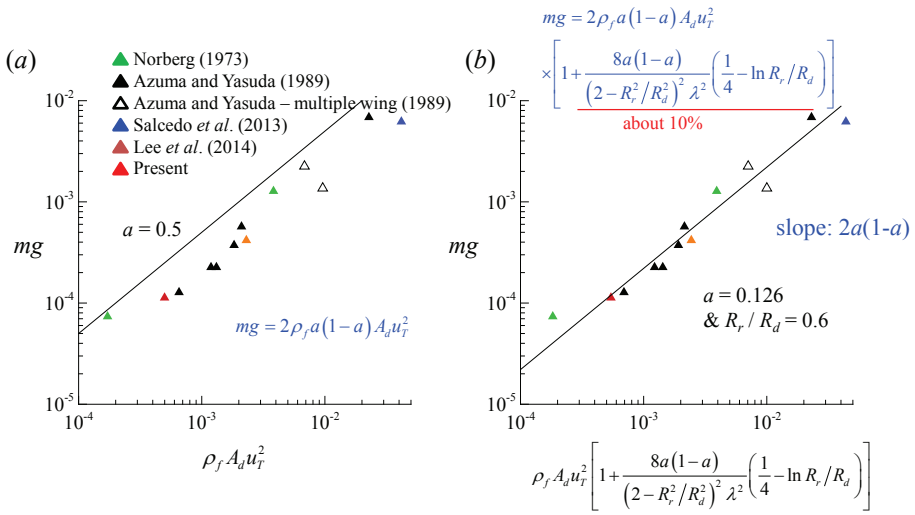

Figure 4.9. Weight versus scaling parameter (a) previous model based on linear momentum theory (Azuma & Yasuda, 1989); (b) present model.

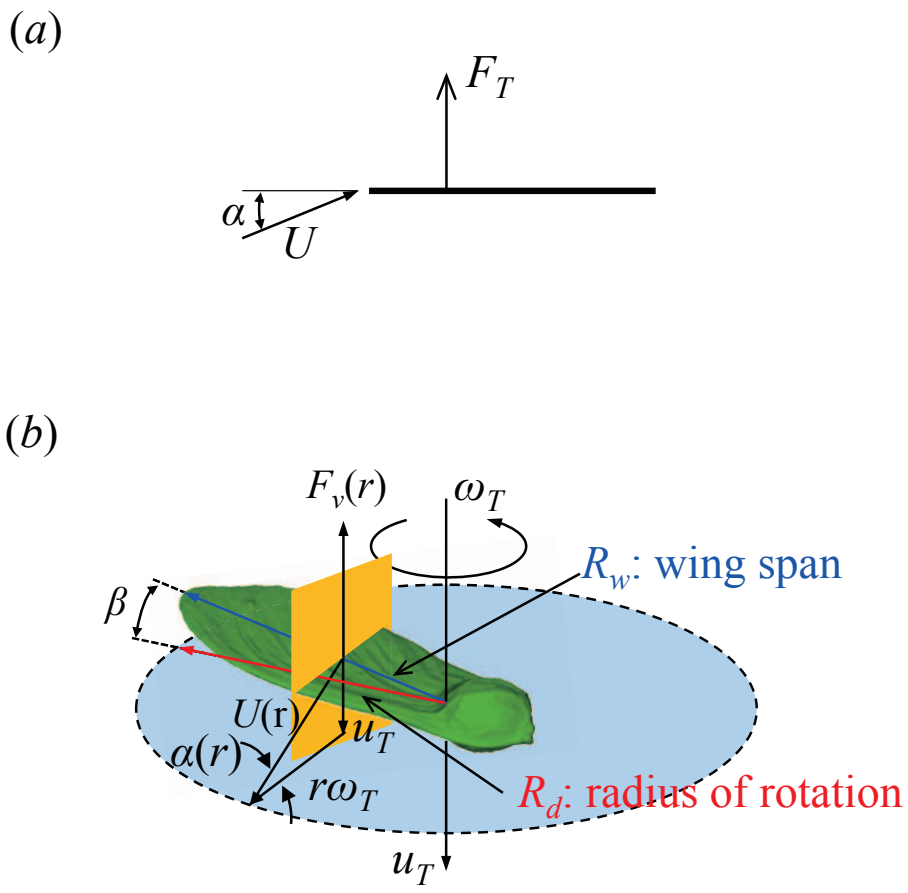

Figure 4.10. (a) Schematic diagram of the circulatory total force of the wing section with respect to incoming velocity U with angle of attack α; (b) schematic diagram for the sectional drag on the rotating wing.

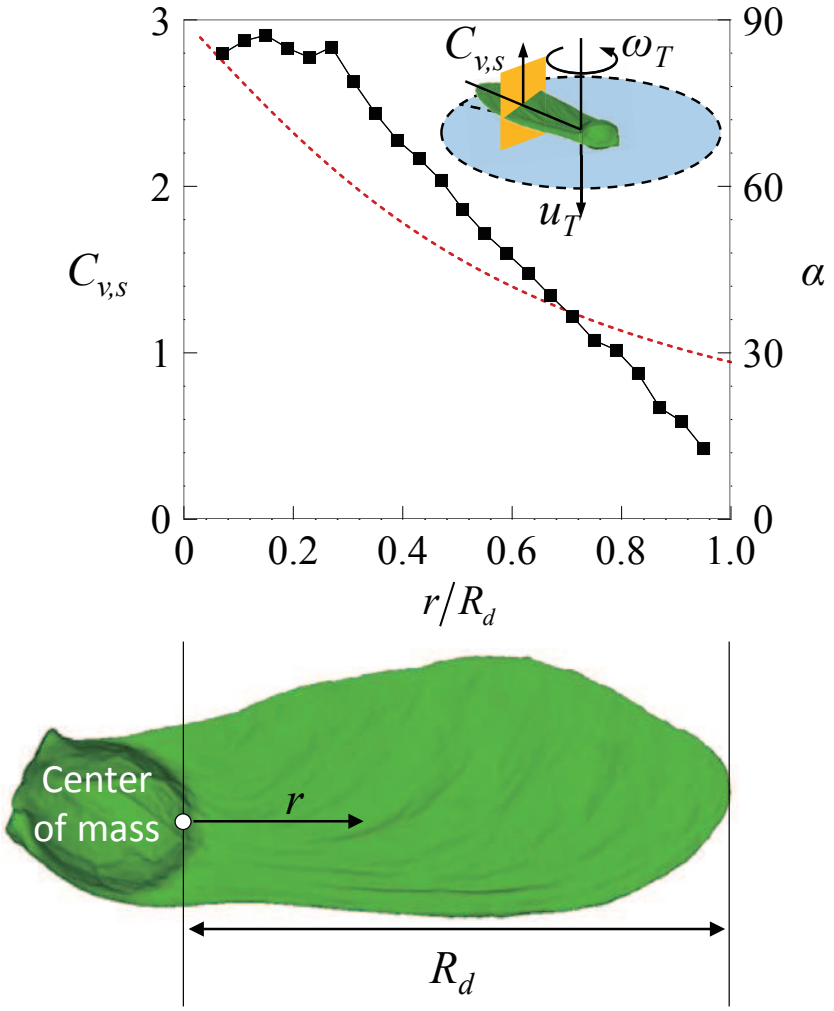

Figure 4.11. Variations of sectional drag coefficient and corresponding angle of attack of the wing section.

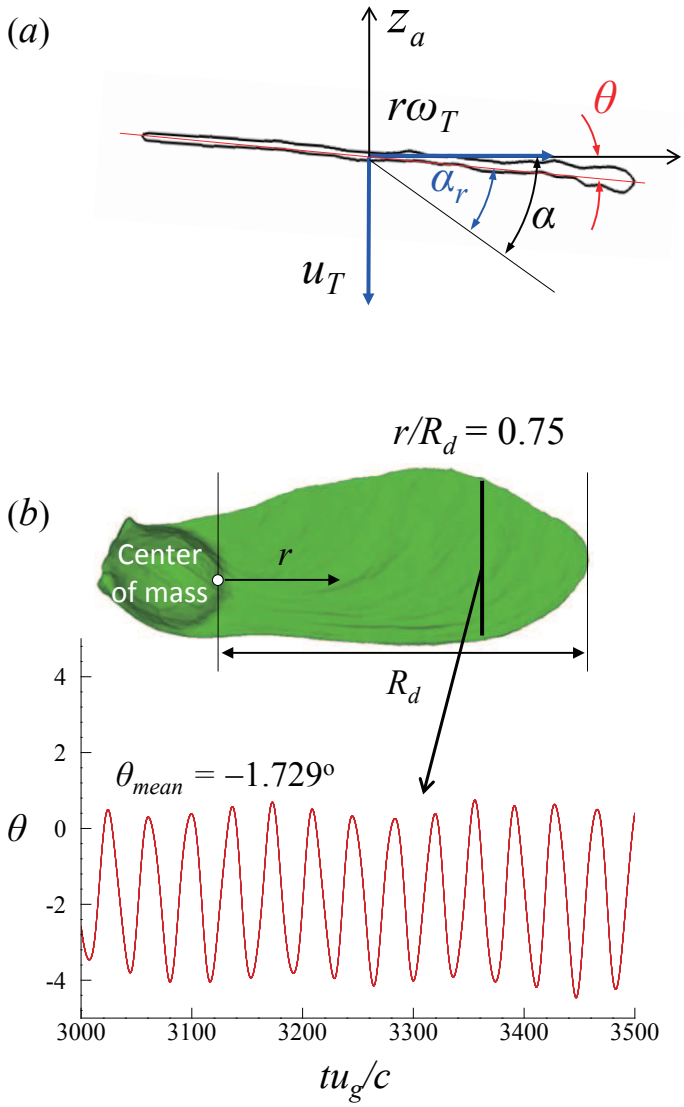

Figure 4.12. (a) Schematic diagram for the definition of angle of attack and pitching angle at a wing section; (b) time trace of the pitching angle at r/R_d =0.75.

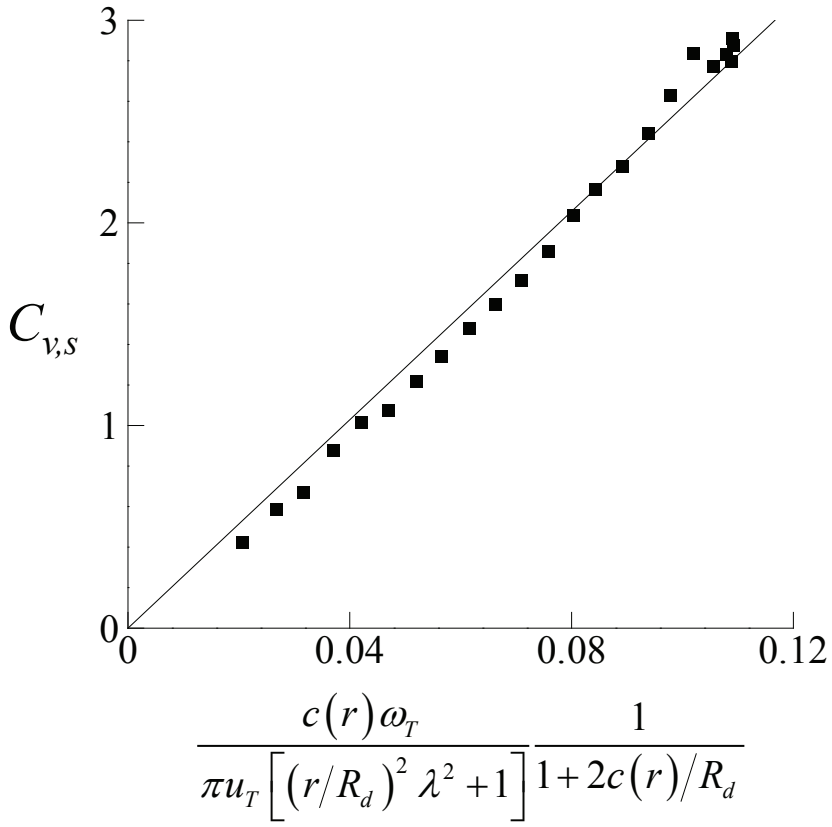

Figure 4.13. Sectional drag coefficient according to the dimensionless scaling law.

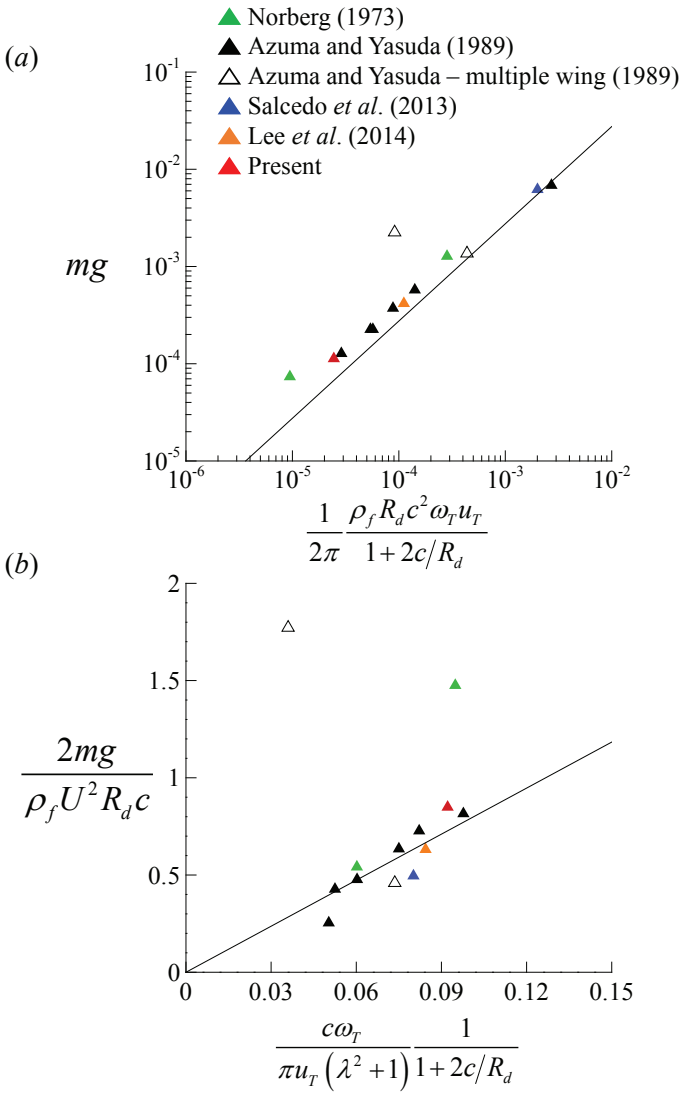

Figure 4.14. Relation between weight of the various seeds and scaling parameters: (a) experimental validation of the scaling law; (b) experimental validation of the normalized scaling law.

Chapter 5

Concluding Remarks

In the present study, a numerical study was conducted to investigate the flows around a freely-falling maple seed. For this purpose, three-dimensional numerical simulations were conducted with a seed model by scanning a maple seed (*Acer palmatum*) using an immersed boundary method in a non-inertial reference frame (Kim & Choi, 2006), which requires much less grid points for resolving fluid motions near the moving body than that in an inertial reference frame (Kweon & Choi, 2010). After a transient period, the seed descended with a periodic rotating motion (helix shape) and its descending velocity decreased rapidly. Then the seed reached the periodic state with its terminal descending and rotating velocities. With the same maple seed, a free-fall test was conducted to obtain its terminal descending and rotating velocities for a validation. The measured terminal descending and rotating velocities were in good agreement with those of high-fidelity numerical simulation indicating the accuracy of the present study. In the periodic state, due to the rotating motion, the leading-edge, trailing-edge, wing-tip, and wing-root vortices were generated as similar to those of hovering insect wing (Kweon & Choi, 2010). Especially, the leading-edge vortex remained stable along the wing surface rather than sheds into the wake, which is known to create high drag force. The leading-edge vortex was most prominent near the base (nut) of the maple seed, but it merged with the tip vortex near the wing tip, resulting in a long trail of vorticity in the wake, and

the strong spanwise flows on the wing surface of the seed were also observed. To further understand the flow characteristics around the autorotating seed, the sectional drag coefficient was also investigated. By integrating the sectional drag force, it was found that the portion of drag force acting on the wing (center of mass to wing tip) is about 9 times greater than that on the nut (base to center of mass) indicating the rotating wing play a prominent role in generating the drag force. Additional simulations were also conducted to investigate the effect of the initial postures on the entrance into autorotation. For this purpose, leading-edge upward, trailing-edge upward, nut upward, and wing-tip upward cases were also simulated in addition to the wing-surface upward case. The autorotation occurred earlier when the leading-edge or nut was initially positioned upward than when the wing tip was positioned upward, and this means that the natural initial posture of the seed may effective for faster entrance into autorotation and also for the conservation of species. The effect of the presence of the wind was also conducted using same seed model. With increasing the magnitude of the wind velocity, the flying velocities of the seed increased and reached at almost same values of the wind. As similar to those of freely-falling maple seed in the quiescent condition, initially the descending velocity increased almost linearly, and then decreased as the rotating velocity increased. Later, the seed model reached a periodic state with terminal descending and rotating velocities. From the instantaneous three-dimensional vortical structures around the seed model, the leading-edge vortex also remains stable along the span rather than sheds into the wake and creates high drag force for all cases considered meaning that the autorotating seed retain its inherent characteristics of stable leading edge vortex on the wing regardless of the effect of wind.

Two different theoretical approaches were considered to obtain scaling laws describing the relation among the seed weight and geometry, and descending

and rotating velocities. The first uses the conservation of mass, linear and angular momentum, and energy. In this approach, a model constant to be determined, called the axial induction factor, is obtained from the result of present simulation. The second approach employs a classical steady wing theory in which the vortical strength is scaled with the circulation around a wing and the lift force is modeled by the time derivative of vortical impulse. Available data from winged seeds are applied to the present scaling laws, showing excellent collapses onto the scaling laws. The model can offer a simple and powerful guideline for biologists and engineers who seek the evolutionary direction of morphologies and kinematics of autorotating seeds and design autorotation-based MAVs, respectively.

References

Alexander, D. E. & Vogel, S. 2003 Nature flyers: birds, insects, and the biomechanics of flight. The Johns Hopkins University Press.

Augspurger, C. K. 1986 Morphology and dispersal potential of wind-dispersed diaspores of neotropical trees. *Am. J. Bot.* **73**, 353–363.

Azuma, A. & Okuno, Y. 1987 Flight of a samara, *Alsomitra macrocarpa*. *J. Theor. Biol.* **129**, 263–274.

Azuma, A. & Yasuda, K. 1989 Flight performance of rotary seeds. *J. Theor. Biol.* **138**, 23–53.

Birch, J. M. & Dickinson, M. H. 2001 Spanwise flow around the attachment of the leading-edge vortex on insect wings. *Nature* **412**, 729–733.

Burke, J. D. 1988 Atmospheric autorotating imaging device. NASA Case No. NPO-17390-I-CU.

Burrows, F. M. 1975 Wind-borne seed and fruit movement. *New Phytol.* **75**, 405-418.

Crimi, P. 1988 Analysis of samara-wing decelerator steady-state characteristics. *J. Aircr.* **25**, 41–47.

Dewey, P. A., Boschitsch, B. M., Moored, K. W., Stone, H. A. & Smiths, A. M. 2013 Scaling laws for the thrust production of flexible pitching panels. *J. Fluid Mech.* **732**, 29–46.

Diaz-Silva, R. A., Sarigul-Klijn, M. M. & Sarigul-Klijn, N. 2013 Rotary decelerators for spacecraft: historical review and simulation results. *AIAA Paper* 2013-5361.

Dickinson, M. H. 1996 Unsteady mechanisms of force generation in aquatic and aerial locomotion. *Am. Zool.* **36**, 537-554.

Ellington, C. P., van den Berg, C., Willmott, A. P. & Thomas, A. L. R. 1996 Leading-edge vortices in insect flight. *Nature* **384**, 626-630.

Engels, T., Kolomenskiy, D., Schneider, K., Lehmann, F.-O. & Sesterhenn, J. 2016 Bumblebee flight in heavy turbulence. *Phys. Rev. Lett.* **116**, 028103.

Fregene, K. & Bolden, C. L. 2010 Dynamics and control of a biomimetic single-wing nano air vehicle. *American Control Conference Paper* WeA01.6.

Green, D. S. 1980 The terminal velocity and dispersal of spinning samaras. *Am. J. Bot.* **67**, 1218-1224.

Glauert, H. 1935 Aerodynamic theory. *Springer* **4**.

Hedrick, T. L. 2008 Software techniques for two- and three-dimensional kinematic measurements of biological and biomimetic systems. *Bioinsp. Biomim.* **3**, 034001.

Hunsaker, D. F. & Phillips, W. F. 2013 Momentum theory with slipstream rotation applied to wind turbines. *AIAA paper* AIAA 2013-3161.

Jakubik, P., Suomela, J., Vainio, M & Ylikorpi, T. 2004 ARIADNA AO4532-03/6201 Final Report. Helsinki University of Technology, Finland.

Jameson, S., Frenene, K., Chang, M., Allen, N., Youngren, H. & Scroggins, J. 2012 Lockheed martin's samarai nano air vehicle: challenges, research, and realization. *AIAA Paper* 2012-0584.

Jeong, J. & Hussain, F. 1995 On the indentification of a vortex. *J. Fluid Mech.* **285**, 69–94.

Kim, D. & Choi, H. 2006 Immeresd boundary method for flow around an arbitrarily moving body. *J. Comput. Phys.* **212**, 662–680.

Kim, J., Kweon, J. & Choi, H. 2015 Sectional lift coefficient of a rotating wing at low Reynolds numbers. *J. Mech. Sci. Tech.* **29**, 4775-4781.

Kim, J., Kim, D. & Choi, H. 2001 An immersed-boundary finite-volume method for simulations of flow in complex geometries. *J.Comput. Phys.* **171**, 132–150.

Kweon, J. 2011 Three-dimensional vortical structures around the flapping insect wings. Seoul National University, Seoul Korea.

Kweon, J. & Choi, H. 2010 Sectional lift coefficient of a flapping wing in hovering motion. *Phys. Fluids* **22**, 070703.

Lee, B., Park, H. & Kim, S.-T. 2015 Three-dimensional wing behaviors of a rhinoceros beetle during takeoff flights. *J. Mech. Sci. Tech.* **29**, 5281–5288.

Lee, E.-J. & Lee, S.-J. 2016 Effect of initial attitude on autorotation flight of maple samaras (Acer palmatum). *J. Mech. Sci. Tech.* **30**, 747–747.

Lee, I.& Choi, H. 2015 A discrete-forcing immersed boundary method for the fluid-structure interaction of an elastic slender body. *J. Comput. Phys.* **280**, 529–546.

Lee, J., Choi, H. & Kim, H.-Y. 2015 A scaling law for the lift of hovering insects. *J. Fluid Mech.* **782**, 479–490.

Lee, J., Park, Y.-J., Jeong, Y., Cho, K.-J. & Kim, H.-Y. 2013 Wake and thrust of an angularly reciprocating plate. *J. Fluid Mech.* **720**, 545–557.

Lee, S. J., Lee, E. J. & Sohn, M. H. 2014 Mechanism of autorotation flight of maple samaras (*Acer palmatum*). *Exp. Fluids* **55**, 1718.

Lentink, D. & Dickinson, M. H. 2009 Rotational accelerations stabilize leading edge vortices on revolving fly wings. *J. Exp. Biol.* **212**, 2705–2719.

Lentink, D., Dickson, W. B., van Leeuwen, J.L & Dickinson, M. H.

2009 Leading=edge vortices elevate lift of autorotating plant seeds. *Science* **324**, 1438–1440.

Limacher, E. & Rival, D. E. 2015 On the distribution of leading-edge vortex circulation in samara-like flight. *J. Fluid Mech.* **776**, 316–333.

Lugt, H. J. 1983 Autorotation. *Ann. Rev. Fluid Mech.* **15**, 123-147.

McCutchen, C. W. 1977 The spinning rotation of ash and tulip tree samaras. *Science* **197**, 691-692.

Minami, S. & Azuma, A. 2003 Various flying modes of wind-dispersal seeds. *J. Theor. Biol.* **225**, 1–14.

Morino, L., Bharadvaj, B. K., Freedman, M. I. & Tseng, K. 1989 Boundary integral equation for wave equation with moving boundary and application to compressible potential aerodynamics of airplanes and helicopters. *Comput. Mech.* **4**, 231–243.

Nathan, R., Katul, G., Horn, H. S., Thomas, S. M., Oren, R., Avissar, R., Pacala, S. W. & Levin, S. A. 2002 Mechanisms of long-distance dispersal of seeds by wind. *Nature* **418**, 409–413.

Newmann, J. N. 1977 Marine hydrodynamics. MIT Press.

Norberg, R. Å. 1973 Autorotation, self-stability, and structure of single-winged fruits and seeds (samaras) with comparative remarks on animal flight. *Biol. Rev.* **48**, 561–596.

Pandolfi, C. & Izzo, D. 2013 Biomimetics on seed dispersal: survey and insights for space exploration. *Bioinspir. Biomim* **8**, 025003.

Park, H. & Choi, H. 2010 Aerodynamic characteristics of flying fish in gliding flight. *J. Exp. Biol.* **213**, 3269–3279.

Phillips, W. F. 2002 Propeller momentum theory with slipstrem rotation. *J. Aircr.* **39**, 184–187.

Pounds, P. E. I. & Singh, S. P. N. 2013 Integrated electro-aeromechanical structures for low-cost, self-depolying environment sensors and disposable UAVs. *IEEE Paper* 4459–4466.

Rao, M., Hoysall, D. C. & Gopalan, J. 2014 Mahogany seed - a step forward in deciphering autorotation. *Curr. Sci.* **106**, 1101–1109.

Rosen, A. & Seter, D. 1991 Vertical autorotation of a single winged samara. *J. Appl. Mech.-Trans. ASME* **58**, 1064–1071.

Rosen, A. & Seter, D. 1992 Stability of the vertical autorotation of a single-winged samara. *J. Appl. Mech.-Trans. ASME* **59**, 1000–1008.

Salcedo, E., Treviño, C., Vargas, R. O. & Martínez-Suástegui, L. 2013 Stereoscopic particle image velocimetry measurements of the three-dimensional flow field of a descending autorotating mahogany seed (*Swietenia macrophylla*). *J. Exp. Biol.* **216**, 2017–2030.

Sane, S. P. & Dickinson, M. H. 2001 The control of flight force by a flapping wing: lift and drag production. *J. Exp. Biol.* **204**, 2607–2626.

Seter, D. & Rosen, A. 1992 Study of the vertical autorotation of a single winged samara. *Bio. Rev.* **67**, 175–197.

Seter, D. & Rosen, A. 2014 Theoretical and experimental study of axial autorotation of simple rotary decelerators. *J. Aircr.* **51**, 236-248.

Smith, E. H. 1971 Autorotating wings: an experimental investigation. *J. Fluid Mech.* **50**, 513-534.

Sørensen, J. N. 2016 General momentum theory for horizontal axis wind turbines. *Springer*.

Sunada, S., Ide, A., Hoshino, Y. & Okamoto, M. 2015 A study of autorotating plant seeds. *J. Theor. Biol.* **386**, 55–61.

Varshney, K., Chang, S. & Wang, Z. J. 2012 The kinematics of falling

maple seeds and the initial transition to a helical motion. *Nolinearlity* **25**, C1–C8.

Varshney, K., Chang, S. & Wang, Z. J. 2013 Unsteady aerodynamic forces and torques on falling parallelograms in coupled tumbling-helical motions. *Phys. Rev. E* **87**, 053021.

Yasuda, K. & Azuma, A. 1997 The autorotation boundary in the flight of samaras. *J. Theor. Biol.* **185**, 313-320.

자유낙하하는 단풍씨앗의 수치해석 연구

서울대학교 대학원
기계항공공학부
이인재

요 약

단풍씨앗과 같이 날개를 지닌 많은 씨앗들은 그들의 종의 보존을 위하여, 자동회전을 활용하여 낙하속도를 감소시키고 그에 따른 확산거리를 증가시키게 된다. 곤충 비행의 경우 구동을 위한 신경근육을 필요로 하는 것과 달리, 이러한 씨앗들은 단순한 구조를 지니고 있으며, 심지어 그 날개가 손상되어도 자동회전을 할 수 있다. 이는 자동회전하는 씨앗들이, 퍼덕이거나 회전하는 블레이드에 의한 메커니즘에 비하여 물리적으로 강건한 형상을 지니는 것을 의미하며, 이로 인해 많은 연구자들이 정찰, 무기, 그리고 대기관찰 등의 목적을 지닌 센서 결합형 소형무인비행체의 개발을 유발하였다.

본 연구에서는 자유낙하 하는 단풍씨앗(*Acer Palmatum*)주위 유동 해석을 위하여 비관성 좌표계의 가상경계 방법을 이용한 고정밀 수치해석을 수행하였다. 이를 위한 3차원 씨앗 모델은 실제 단풍 씨앗을 스캔함으로써 얻게 된다. 일시적인 구간을 지나 씨앗은 안정한 상태의 자동회전 구간에 도달하였다. 이 때 일시적인 구간은 씨앗의 초기자세에 의존하는 것을 보였으며, 씨앗 날개의 전단 및 끝단, 혹은 열매가 위로 향하였을 때 더 짧아지는 것을 보였다.

씨앗의 무게와 형태, 그리고 낙하 및 회전속도간의 관계를 설명하는 스케일링 법칙을 구하기 위해 두 가지의 다른 접근법이 고려되었다. 첫 번째 방법은 질량, 선형 및 각운동량, 그리고 에너지 보존을 이용하였다. 여기에서 유도되는 모델상수(axial induction factor)는 본 연구의 결과로부터 얻어진다. 두 번째 방법은 기존의 정상 날개 법칙(steady wing theory)을 도입하였으며, 여기에서 와도의 세기는 날개 주위의 순환(circulation)에 의해 스케일링 되며 양력은 와도의 임펄스의 시간에 대한 미분으로부터 모델링 된다. 날개 달린 씨앗들의 측정된 데이터들을 본 스케일링 법칙에 적용하였으며, 스케일링 법칙에 매우 잘 일치하는 것을 확인하였다. 이러한 이론적 분석들은 자동회전하는 씨앗의 형태학과 운동역학적 진화의 방향을 찾는 연구자들이나 자동회전 기반의 소형무인비행체를 개발하는 연구자들에게 간단한 지침을 제시해 줄 수 있을 것이다.

……

주요어: 단풍씨앗, 자동회전, 전단와류, 스케일링법칙, 운동량이론, 날개이론
학 번: 2008-20774